Herbert Oertel

Modelling the Human Cardiac Fluid Mechanics

universitätsverlag karlsruhe

Modelling the Human Cardiac Fluid Mechanics

von
Herbert Oertel

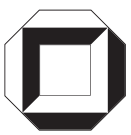

universitätsverlag karlsruhe

Autor

Prof. Prof. e.h. Dr.-Ing. habil. Herbert Oertel, Ordinarius
Institut für Strömungslehre, Universität Karlsruhe (TH)
Kaiserstr. 12, 76128 Karlsruhe

Impressum

Universitätsverlag Karlsruhe
c/o Universitätsbibliothek
Straße am Forum 2
D-76131 Karlsruhe
www.uvka.de

Universitätsverlag Karlsruhe 2005
Print on Demand

ISBN 3-937300-82-1

Modelling the Human Cardiac Fluid Mechanics

H. Oertel *

Institute for Fluid Mechanics, University of Karlsruhe, D-76128 Karlsruhe, Germany

Abstract

We present a virtual heart model simulating the flow in the left human ventricle and in the aorta. Because of the lack of *in vivo* structure data of the human ventricle, the active ventricle movement is given by a time-dependent ventricle model that is derived from *in vivo* image data of a nuclear spin MRT tomograph of a healthy human heart. The passive part of the virtual heart model consists of a model aorta and vena cava, and of heart valves. As the movement is due to the flow in the inactive region of the heart, a coupling of flow and structure is necessary in the model to take into account the deviation of the aorta and the closing and opening of the heart valves. The flow calculation is performed with a finite volume method, while the structure of the aorta is calculated using the finite element method. The flow resistance of the time simulation in the body is taken into account with a circulation model. In the outlook of the article, we show how the virtual heart model can be used to predict flow losses due to pathological ventricle contraction defects in an unhealthy human heart.

1 Introduction

To calculate the flow in the human heart, we need to model the time-dependent geometry of the ventricle and of the heart valves during one cardiac cycle. In the literature many approaches that model the electro-mechanical pump behavior of the heart are found. The structure of the muscle fibers of the human heart was published by Robb and Robb already in 1942. Hunter et al. (1996a), (1996b), (1998) developed the finite elasticity theory and a finite

* Corresponding author.
Email address: oertel@isl.mach.uni-karlsruhe.de (H. Oertel).
URL: www-isl.mach.uni-karlsruhe.de (H. Oertel).

element method for analyzing ventricular electro-mechanics during the filling phase of the cardiac cycle, when cardiac muscle cells are not actively contracting. The orthotropic properties of the passive tissue are described by a constitutive law, whose parameters are derived from a model of collagen fibers and *in vitro* stress measurements on animal hearts. A model of the active tissue properties, based on isolated animal muscle experiments, is also introduced in order to predict transmutal distributions of principal strain at the end of the contraction phase of the cardiac cycle.

The calculation of the flow-structure coupling of the heart was introduced by Peskin and McQueen (1997), (2001). It approximates the muscle fibers of the heart as well as the cardiac valves in the Lagrangian description with discrete elastic fiber filaments embedded in the flow. The discretization of the fiber filaments is chosen to be so fine that they have no volume or mass, but can still be used for a continuum mechanical description of the material. The filaments are oriented along the flow and have local flow velocities. At each point of the filament-flow combination, a unique fiber direction is given. The degree of detail of the model structure is very high, and in particular the structure of the heart valves is modelled very precisely. The method was further developed by Lemmon and Yoganathan (2000), and applied with a simplified model to the left cardiac ventricle for the filling phase of the cardiac cycle.

Watanabe et al. (2002) chooses another approach of the flow-structure coupling of the heart, based on a simplified electro-physical and muscle contraction model. The coupling of the flow with the mechanical structure model of the cardiac muscle takes place via the pressure.

Common to all work is that the structure model of the heart is based on *in vitro* measurements on animal hearts, which cannot be carried over to the living human heart. This is the point where our virtual heart model for the flow simulation in the heart ventricles comes into play, Oertel (2004), Oertel et al. (2004). The model does without the structure calculation of the ventricle myocardium and derives the time-dependent geometry model of the ventricle that is necessary for the flow calculation from nuclear spin tomography image data of the healthy human heart. This also has the advantage that the virtual heart model can also be used for the flow calculation of pathological ventricle defects of unhealthy human hearts. The calculation of the passive part of the heart model with the aorta and vena cava is carried out using a simplified linear model of the flow-structure coupling, Schenkel et al. (2003a).

Every minute the human heart pumps about 5 l of blood into the circulation. If the body is under duress, the pump efficiency can increase to 20 to 30 l per minute. The human heart consists of two separate pump chambers, the left and right *ventricles* and *atria* which are made out of cardiac muscle (Fig. 1). The right atrium contains blood which is weak in oxygen following systemic circulation. The right ventricle subsequently fills with blood from the right atrium, and then empties again into the pulmonary circulation on contraction. The reoxygenated blood from the pulmonary circulation reaches the left atrium and is passed along from the left ventricle into the systemic circulation. The atria and ventricles are separated by atrioventricular valves which regulate the filling of the heart ventricles. The right valve has three flaps and is therefore called the *tricuspid valve*. The left bicuspid valve has two flaps and is known as the *mitral valve*. The flaps ensure that the atria can fill with blood between the heart beats and prevent backflow of the blood when the ventricles contract. While the ventricles relax, the *pulmonary valve* prevents backflow of blood out of the aorta into the left ventricle.

During one cardiac cycle (Fig. 2), the ventricles carry out a periodic contraction and relaxation. This pump cycle is associated with changes in the

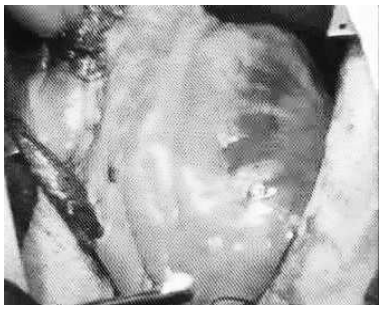

Beyersdorf, 2003

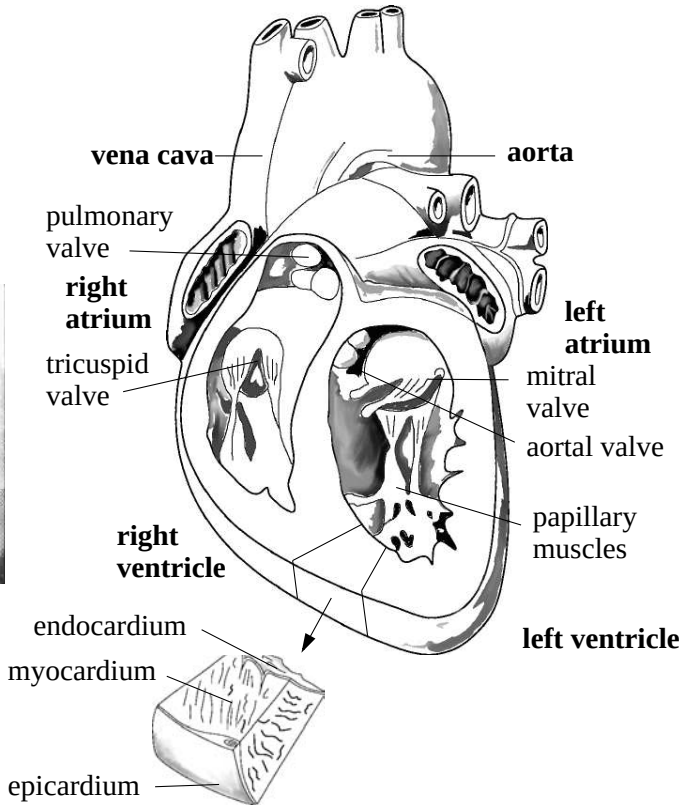

Fig. 1. Human heart

ventricle and artery pressures. Figure 3 shows the pressure in the left and right chamber of the heart. The entire cycle can be split into four phases (Fig. 4). The isovolumetric ventricle contraction is called the filling phase (1) and contraction phase (2), and the isovolumetric ventricle relaxation is called the expulsion phase (3) and relaxation phase (4). Phases (2) and (3) of the ventricle contraction are called *systole* and phases (4) and (1) of the ventricle relaxation are called *diastole*. The ventricle is filled during phase (4). The pressure at this point is only slightly higher in the left atrium than in the left ventricle. The mitral valve is therefore open and the blood flows out of the pulmonary veins into the atrium and on into the left ventricle. As the filling volume increases and the ventricle expands, the ventricle pressure increases. The pressure in the aorta is considerably larger, so the aortal valve remains closed. The arterial pressure sinks continuously during the subsequent diastole, corresponding with the blood flow into the arterial vascular system. With the start of the ventricle contraction, the ventricle pressure increases above that of the atrium, so that the bicuspid valve closes. When the valve is closed, the ventricle contracts to retain a constant blood volume. While this increases the ventricle pressure to 166 mbar, the pressure decrease in the arteries continues. The aortal valve is opened when the ventricle pressure exceeds that in the

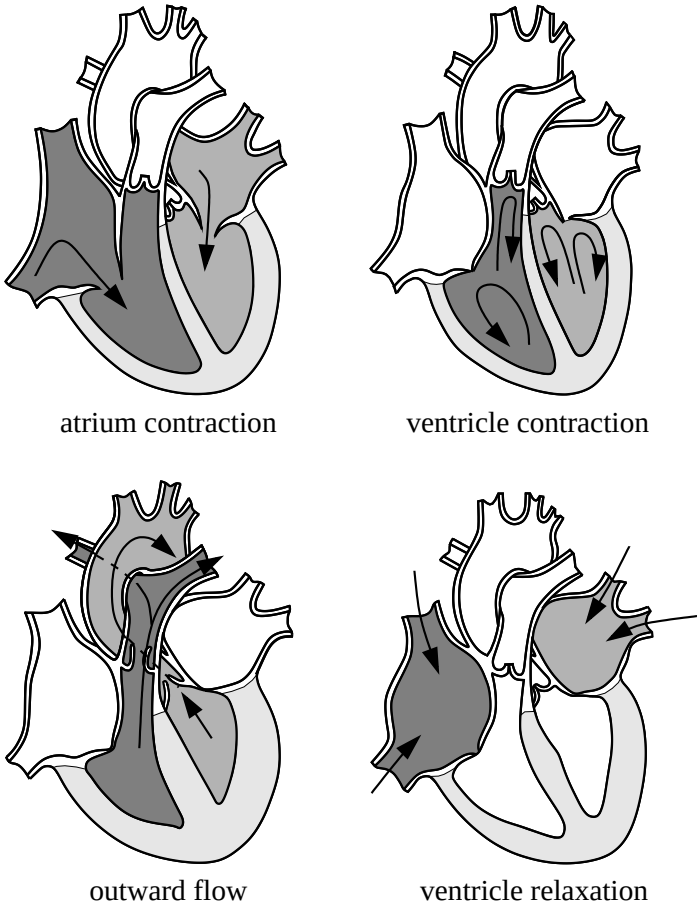

Fig. 2. Four phases of the cardiac cycle

aorta. Now a constant quantity of blood is forced out into the aorta. While the constant blood volume in the aorta is forced, the aortal pressure increases from its minimum value of 107 mbar to its maximum value of 160 mbar. After ventricle relaxation has begun, the ventricle pressure drops below that of the arteries, and the aortal and pulmonary valves close. The phase of isovolumetric relaxation now follows. The first phase of the diastole goes on as long as the ventricle pressure is below the atrium pressure. Then the mitral valve opens and the cardiac cycle starts the next filling phase.

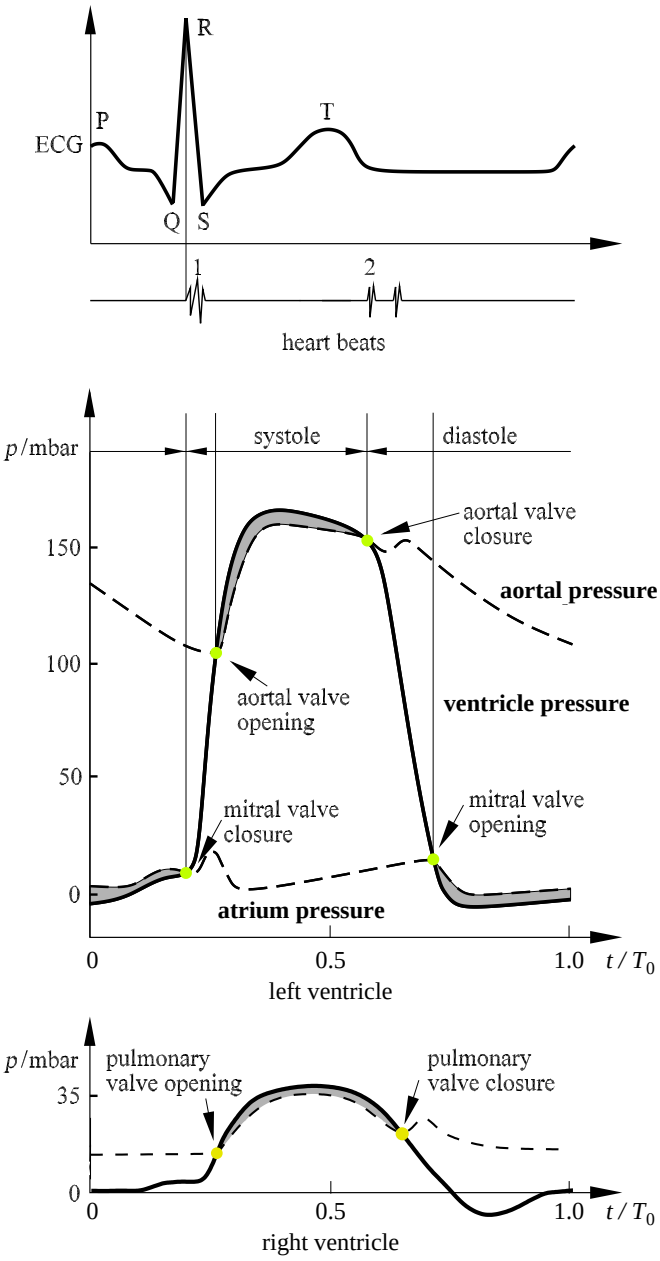

Fig. 3. Echocardiogram (ECG) and pressure in the left and right ventricle, $T_0 = 0.8$ s

The pressure-volume diagram in Figure 4 shows the filling of the left ventricle (1) along the rest expansion curve, the isovolumetric contraction (2), as well as the expulsion of 80 ml blood during each cycle (3) and the isovolumetric relaxation (4). The enclosed surface is the systolic work done by the left heart ventricle. When the body is under duress, the work diagram shifts along the rest expansion curve to large ventricle volumes and higher pressure. Increasing the heart filling leads to an increase in the cardiac work. When the aortal pressure is increased, the aortal valve opens later, so that the isovolumetric contraction phase reaches higher pressures.

The mechanical contraction of the cardiac muscle is controlled by *periodic electrical impulses*. It starts with the excitation of the sinoatrial node, which carries out cyclical electrical depolarization and polarization, and therefore has the function of the primary pace maker. During the depolarization phase, the discharge extends across the conduction paths with a velocity of 1 m/s into the surrounding muscles of the atria, which then contract. The electrical impulse of the sinoatrial node is delayed in the ventricular node. This delay permits optimal filling of the ventricles during contraction of the atria. The impulse passes along the His nerve fibers and the sides of the chamber with a velocity of 1–4 m/s and reaches the ventricle muscles after about 110 ms. In the direction of the ventricle, the bundle of His divides into the left and right

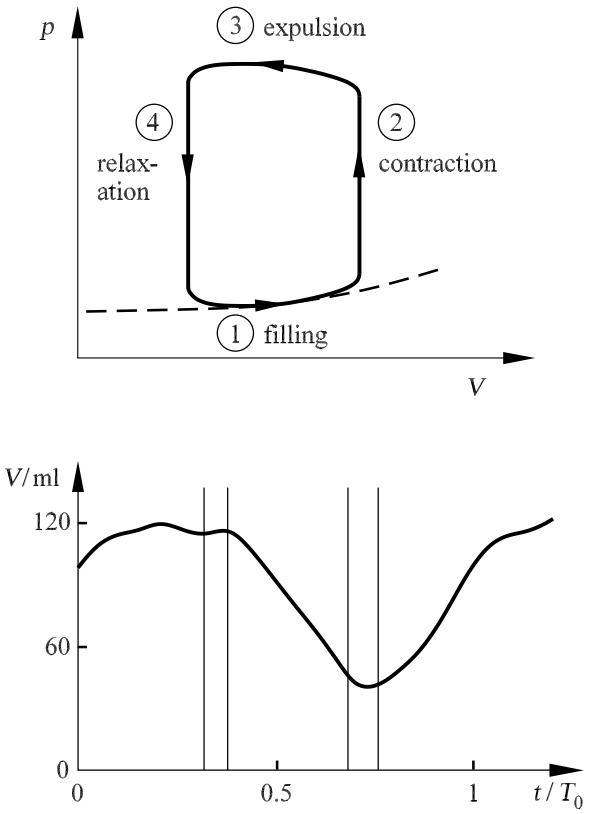

Fig. 4. Pressure-Volume diagram during one cardiac cycle, $T_0 = 0.8$ s

sides of the chamber.

As the ventricles begin to contract, the contraction in the atria is finished, thanks to the delay of the conduction in the ventricular nodes. At this point all nerve cells in the impulse conduction system, apart from the impulse-forming cells in the sinoatrial nodes and ventricular nodes, can be spontaneously depolarized. The ventricular depolarization in the electrocardiogram in Figure 3 takes less than 0.1 s.

The cycle of depolarization and polarization generates a small electrical potential which can be measured on the surface of the body. The depolarization of the atria causes a small deflection, called the P-wave. After a pause of about 0.2 s, this is followed by a strong deflection due to the depolarization of both ventricles (QRS). The T-wave then follows, caused by renewed polarization of the ventricles. The association of the electrical potentials with the mechanical processes and pressure changes in the left ventricle of the heart is also shown in Figure 3.

As the mitral valve closes, the pressure in the left ventricle rises. This is associated with a sound wave which is detected as the first heart beat. This induces the systole, the contraction of the ventricle. At the second heart beat the diastole, the phase of ventricle relaxation, begins.

The overall flow in the left ventricle during one ventricle cycle is shown in Figure 5. When the mitral valve opens, a jet intake flow forms in the ventricle at the beginning of the filling process of the left ventricle. After one quarter of

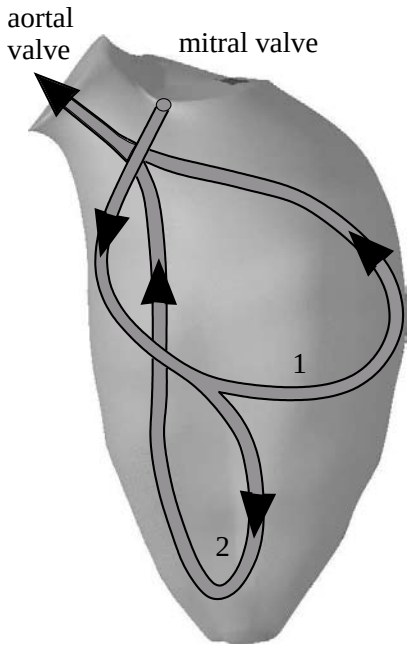

Fig. 5. Cardiac flow in the left ventricle

the cardiac cycle this is accompanied by a ring vortex which moves through the blood at rest in the relaxed ventricle and is slowed down by it. There is no flow through the top of the ventricle at this time. In the rest of the diastole the intake vortex increases in size and is deformed due to the moving edges of the ventricle. After about 0.25 of the cardiac cycle the ring vortex branches, and the blood begins to flow through the top of the ventricle. The branching takes place as shown in Figure 5 such that the direction of the exit flow process through the aortic valve is already determined. The velocity of the three-dimensional branched flow now decreases until the intake flow process is completed and the mitral valve closes. Further deformation of the vortex structure is determined by the inertia of the flow.

When the aortic valve opens after 0.38 of the cardiac cycle, the exit flow process into the aorta begins. A jet flow forms in the aorta. This initially washes away the main flow 1 and then the flow in the top of the ventricle 2. At the end of the systole the vortex structure has completely separated in the left ventricle. In the healthy heart 65% of the ventricle volume is expelled during one cardiac cycle. Total expulsion of the oxygen-rich blood into the aorta takes place over two cardiac cycles.

1.2 Blood Circulation

The *systemic circulation* can be split into three main parts, the blood distribution system, consisting of the *aorta*, large and small *arteries* and *arterioles*. These further divide into the *capillaries*, where gas and material exchange takes place in the micro-circulation by diffusion. The blood flows back to the heart via the venules, small and large *veins* and the *vena cava*.

The mean blood pressure on leaving the left ventricle is about 133 mbar. This drops to 13 mbar when the blood returns to the right ventricle. Figure 6 shows the mean pressure and pressure variations in the different artery regimes. Because of the elastic properties of the aorta, the pressure pulses between 120 mbar and 160 mbar around the mean value. In the large arteries, the amplitude of the pulsation initially increases, because of the wave reflection. It then sinks drastically to a mean value of 40 mbar in the arteriole region over a distance of a few millimeters. In the capillaries and venules, the pressure drop continues less sharply. Eventually there is a pressure of 13 mbar to push the blood back to the right ventricle. In the large veins and the vena cava, there is no pulse and no considerable pressure drop. Simultaneously pressure waves occur which are due to the pulsation of the right ventricle and move in the opposite direction to the flow of blood. The systolic pressure in the pulmonary arteries is quite small, about 20 mbar. A pressure drop of only 13 to 7 mbar is needed in order to overcome the flow drag in the lung volume,

and so 13 to 7 mbar filling pressure remain for the left ventricle.

Because of their elasticity, the aorta and the large arteries act as a so-called *volume reservoir*. The acceleration part of the blood pulse is reduced and a higher pressure level is retained during the diastole and systole. This means that the flow in the arterial branches is smoother.

Between each pressure pulse, the arteries contract by about 5% and so maintain the blood transport. The pressure pulse in the arteries is positive, even during the systole of the heart. In contrast, a backflow occurs in the large arteries for a short time. The flow velocity is zero as the aortic valve is closed. The amplitude of the flow pulse decreases with increasing arterial branches and the pulse width increases while a smaller backflow occurs. The forward motion of the pressure pulse through the arterial branches is initially associated with an increase in the pressure amplitude, which is caused by the arterial branches and also by the decrease in elasticity of the artery wall. The flow profile in the branched arteries becomes more uniform.

The Reynolds numbers formed with the mean velocity are 3400 for the aorta, 500 for the large arteries, 0.7 for the arterioles, $2 \cdot 10^{-3}$ in the capillaries, 0.01 in the venules, 140 in the large veins and 3300 in the vena cava. The beating of the heart causes a periodic laminar flow in the smaller arteries and a transitional flow in the larger arteries and the aorta. The transition to turbulent flow takes place over a short time in the turning points of the velocity profile, close to the walls of the arteries. However, because of the shortness of the flow pulse the local transition to turbulence in the wall boundary layer cannot take place completely.

In the curved arteries and in particular in the aorta, the centrifugal force causes *secondary flows*. These have a velocity component perpendicular to the streamlines and cause a circulation flow in the direction of the outer wall.

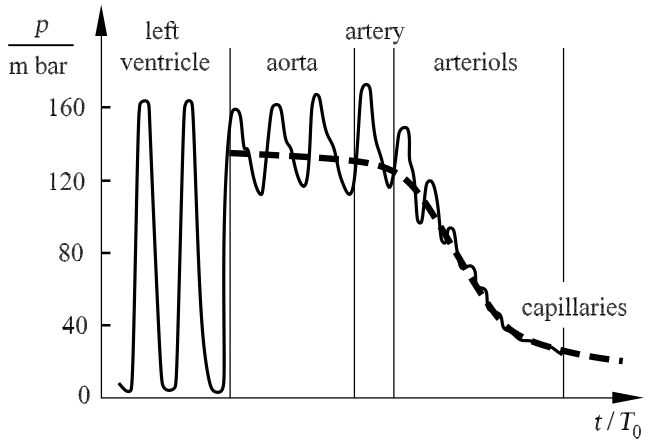

Fig. 6. Pressure in the arterial circulation

Figure 7 shows a snapshot of the velocity distribution in the bend of the aorta taking into account the centrifugal force, the streamline branching in the head, leg and collarbone arteries, and the flow structure of the secondary flow in the descending aorta. At the beginning of the systole, the flow first reaches a maximum at the inner side of the ascending aorta. After passing through the curved and branching region, the velocity maximum moves to the outer side of the aorta curve. Because of the centrifugal force, two secondary vortices arise which remain well into the diastole. Half-way through the cardiac cycle a radial evasive motion of the aorta can be observed. The point of maximum deceleration of the flow is passed through. The velocity profile then flattens and a first backflow is seen in the ascending aorta. Towards the end of the cardiac cycle the aorta has almost fully returned to its original state.

A model of the circulation flow is necessary for the flow simulation in the heart. This should formulate the boundary conditions at the artery exits and the vein entrances of the heart model. The circulation model of Naujokat and Kiencke (2000) takes into account the flow from the left heart ventricle into the aorta and into the attached arterial system of the body circulation, to the venous system, the right heart ventricle, the lung and back to the left ventricle. The circulatory system is divided into i elastic pipe segments. Within the framework of the electrodynamic analogy, whose basis was described by Guyton et al. (1972), the solution of the Navier-Stokes equation for the elastic pipe flow in each segment of the circulation model is found by associating the electric resistance, inductivity and capacity with the physical properties of the arterial and venous branching and the rheological properties of the blood. The flow velocity v and the pressure p correspond to the electrical current

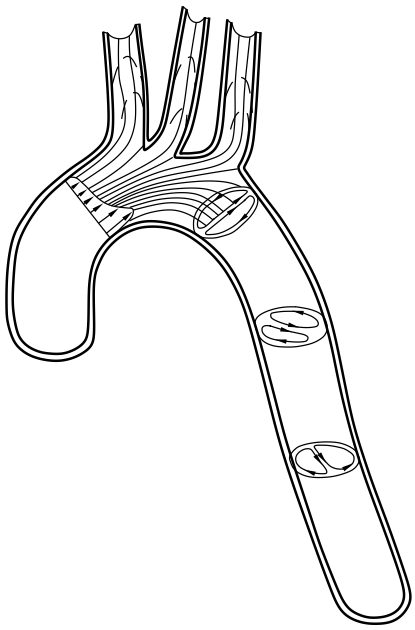

Fig. 7. Secondary flow in the aorta

strength and voltage respectively. In analogy to the solution of the Navier-Stokes equations, for each elastic pipe segment we have the following ordinary differential equations:

$$p_{i-1} - p_i = \frac{9 \cdot \rho \cdot L}{4\pi^2} \cdot \frac{\mathrm{d}v_i}{\mathrm{d}t} + \frac{8 \cdot \mu_{\text{eff}} \cdot L}{\pi r^4} \cdot v_i \tag{1}$$

$$= I \cdot \frac{\mathrm{d}v_i}{\mathrm{d}t} + R \cdot v_i \quad ,$$

$$v_i - v_{i+1} = \frac{3 \cdot \pi \cdot r^3 \cdot L}{2 \cdot E \cdot d} \cdot \frac{\mathrm{d}p_i}{\mathrm{d}t} = C \cdot \frac{\mathrm{d}p_i}{\mathrm{d}t} \quad , \tag{2}$$

with the electric resistance R, the inductivity I and the capacity C. L is the pipe length, r the pipe radius, d the wall thickness of the pipe segment, ρ is the density of the blood and μ_{eff} is the blood viscosity. E is Young's elastic modulus of the pipe segment.

Figure 8 shows the 128 branching and pipe segments of the arterial circulation model. The modelling of the vein and lung circulation is carried out analogously, however with a lesser degree of detail.

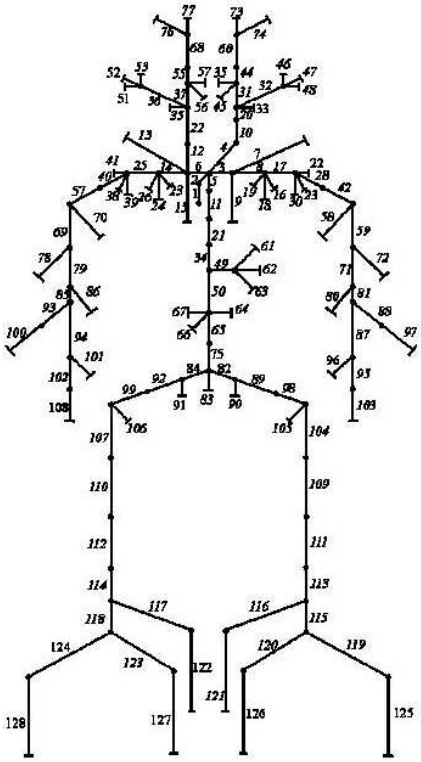

Fig. 8. Circulation model

The *blood* is a suspension consisting of *blood plasma* and 40 to 50 percent of volume of deformable *blood corpuscles*. The red blood corpuscles are deformable disk-like bodies with a length of 8 micrometers. Whereas the blood plasma consists of 90% water and therefore has Newtonian properties, the blood suspension has non-Newtonian properties. To first approximation, the viscous properties of the blood can be described with an effective viscosity μ_{eff}. This increases with decreasing shear rate, due to the increasing accumulation of red blood corpuscles.

The non-Newtonian properties of the blood as it flows through the vessels lead to a reduction of the erythrocytes close to the vessel walls and therefore to a reduction in the viscosity. This alters the velocity profile close to the wall and so also the drag of the blood. Segregation close to the wall leads to a plasma zone which is almost cell-free, and which can be computed with the plasma viscosity μ_{p}.

Figure 9 shows the dependence of the viscosity μ of the blood on the shear rate $\dot{\gamma}$. For the flow in the vessels, the shear rate is $\dot{\gamma} = \partial u/\partial r$. In vascular branches, and in the aorta and ventricles, the dominant component of the shear rate tensor has to be chosen for $\dot{\gamma}$. In a wide range of varying velocity gradients, a drop in the viscosity of up to two orders of magnitude is noted. The region of velocity gradient in a healthy circulation varies between 8000 s^{-1} (arterioles) and 100 s^{-1} (vena cava). Therefore in the asymptotic region the viscosity is almost constant. In the region of very high velocity gradients and therefore very large shear stresses, there is a deformation of the erythrocytes, which itself affects the viscosity of the blood suspension. At shear stresses over 50 n/m^2, the erythrocytes begin to pull apart in a spindle-like manner.

At shear rates of less than 1, such as those which occur in the backflow regions of an unhealthy circulation, aggregation of the erythrocytes occurs. The cells

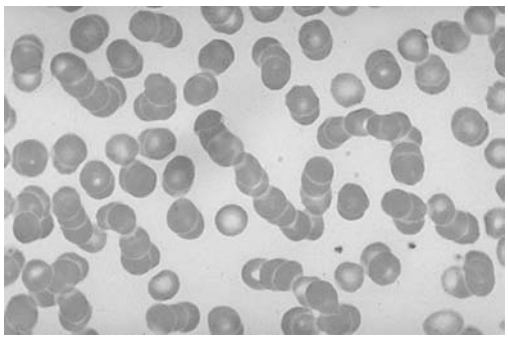

erythrocytes

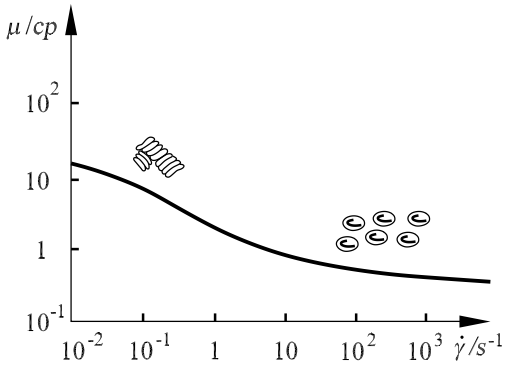

Fig. 9. Blood viscosity

pile up onto one another and form connected cell stacks which are linked together. However, in a healthy circulation system no aggregation can take place in the largest arteries. This is because the aggregation time is about 10 s while the pulse is a factor 10 shorter.

The dependence of the shear stress of the blood τ on the shear rate $\dot{\gamma}$ can be described to good approximation with the *Casson equation*

$$\sqrt{\tau} = \sqrt{\mu_{\text{eff}} \cdot \dot{\gamma}} = K \cdot \sqrt{\dot{\gamma}} + \sqrt{C} \quad . \tag{3}$$

Here K is the Casson viscosity and C the deformation stress of the blood. Fitting this equation to experimental results leads to the equation

$$\sqrt{\frac{\tau}{\mu_{\text{p}}}} = 1.53 \cdot \sqrt{\dot{\gamma}} + 2 \quad , \tag{4}$$

with the plasma viscosity $\mu_{\text{p}} = 0.012$ p. For shear rates larger than 100 the blood behaves as a Newtonian medium.

For the numerical calculation of the pulsing blood flow the modified *Cross model* of Perktold et al. (1991) is used:

$$\mu_{\text{eff}} = \mu_\infty + \frac{\mu_0 - \mu_\infty}{(1 + (t_0 \cdot \dot{\gamma})^b)^a} \quad . \tag{5}$$

The constants $\mu_\infty = 0.03$ p, $\mu_0 = 0.1315$ p, $t_0 = 0.55$ s, $a = 0.3$ and $b = 1.7$ are adapted to the experiments of Liepsch et al. (1991). Here μ_∞ is the limiting viscosity for large shear rates $\dot{\gamma}$ and μ_0 is the limiting viscosity for small shear rates.

1.4 KAHMO Heart Model

The flow simulation in the left human ventricle and in the aorta are carried out using the virtual *KAHMO heart model* (**Ka**rlsruhe **H**eart **Mo**del). The heart model is divided into the *active part* consisting of the cardiac ventricles and the atria and the *passive part* with the aorta and cardiac valves. The human circulation is taken into account with a circulation model.

As there are no *in vivo* structure data of the human ventricle myocardium available, the model does without an active flow-structure calculation in the ventricle and replaces these by *in vivo* measurements of the human ventricle motion with image data from nuclear spin MRT tomography. Figure 10 shows

horizontal sections of the MRT tomograph of a healthy human heart at a given point in time and the geometry model derived from it.

The periodic geometry model of the human heart is represented at each point in time by 26 horizontal and vertical sections. A cardiac cycle consists of 18 time steps with a time resolution of 50 ms of the MRT tomograph. The geometry data of the periodic ventricle motion is recorded over 17 cardiac cycles and converted into a CAD geometry model. The trigger for recording the image takes place via the ECG shown.

The passive part of the KAHMO heart model consists of a model aorta and vena cava, as well as the heart valves. In the inactive part of the heart, in contrast to the ventricles, the movement is caused by the flow. To calculate the pulsing deviation of the aorta and the cardiac valve motion, a flow-structure coupling is therefore necessary. The stress-extension distributions of the aorta and the heart valve flaps necessary for this are taken from the literature.

Supplementary image data and velocity measurements with ultrasonic Doppler echocardiography form the basis to develop a simplified model of the heart valves. Instead of all three-dimensional details of the valve motion, only their projection onto the valve plane is modelled, in such a way that the volume fluxes are correctly represented by the human valves. The three-flap aortic and pulmonary valves are simulated with a variable-aperture cross-section and variable flow resistance, while the two-flap sail valve is simulated with a slit aperture.

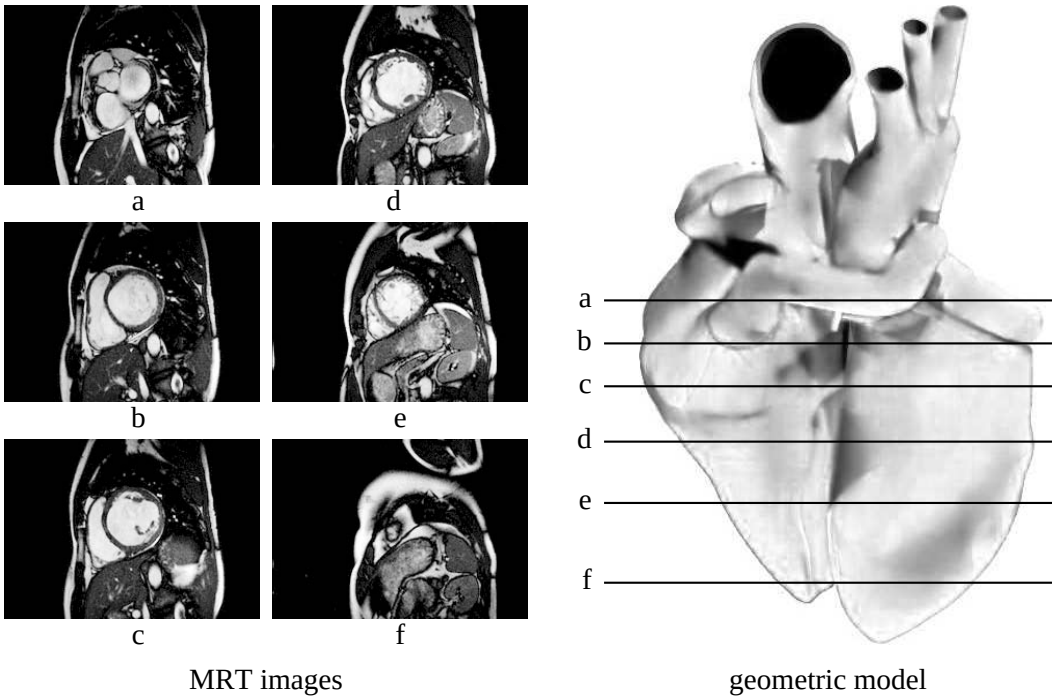

Fig. 10. KAHMO heart model

Figure 11 shows a result of the flow simulation of the following chapter with the KAHMO heart model. The result is for the left ventricle and the model aorta of a healthy human heart at four points in the cardiac cycle. In each case a snapshot is shown of a streamline in the left ventricle projected onto a longitudinal section, as well as the three-dimensional streamline in the aorta. The intake flow into the left ventricle as the mitral valve is opened can be seen, along with the intake vortex that accompanies it. This branches according to Figure 5 into two parts, so that the flow also washes through the top of the ventricle. As the aortic valve is opened, the first part is initially expelled into

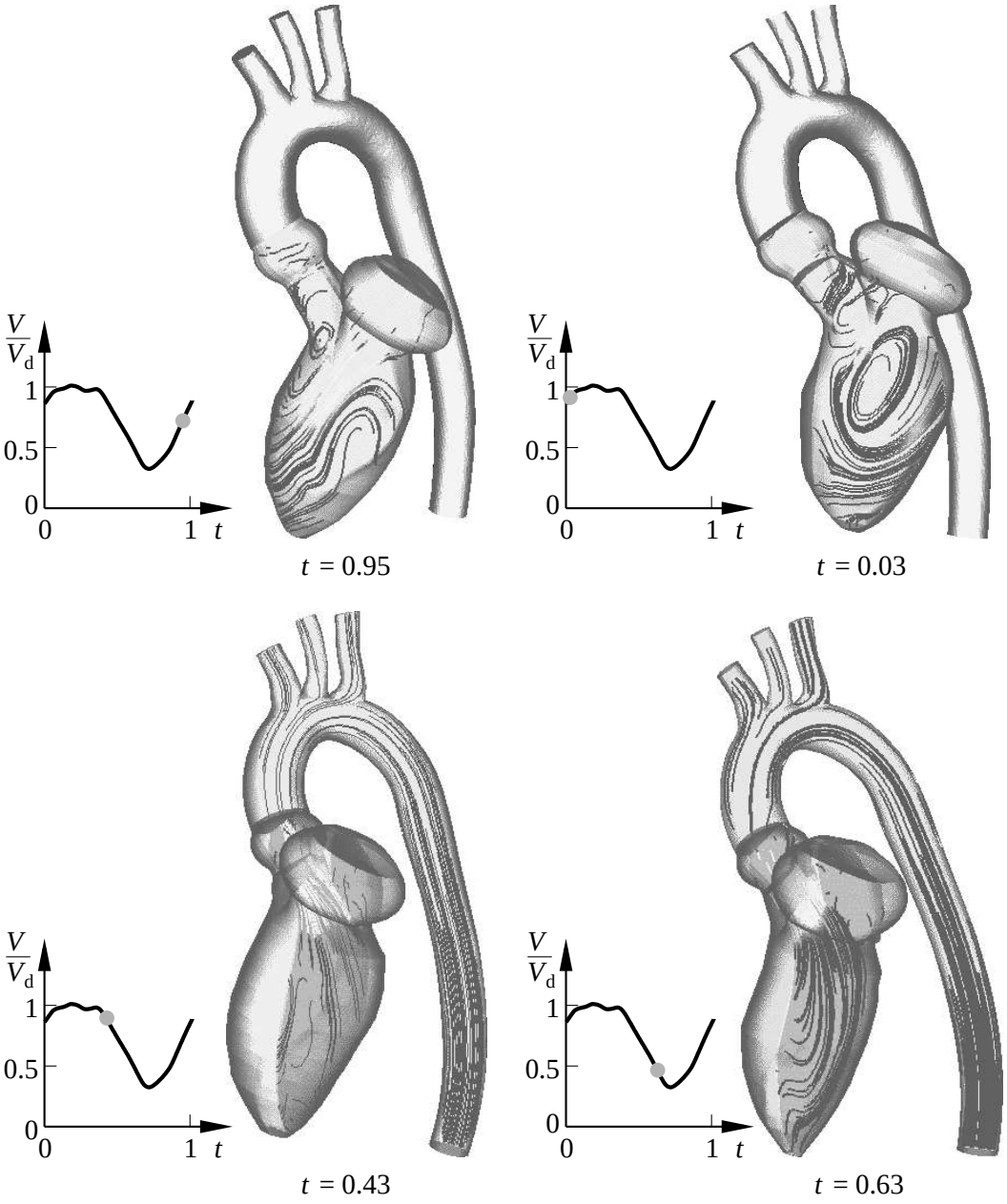

Fig. 11. Flow simulation with the KAHMO heart model, $Re_{D\text{systolic}} = 2739$, $Re_{D\text{diastolic}} = 1079$, $Wo = 25.2$, $t_0 = 0.77$ s

the aorta. The streamlines branch in the aorta into each artery and, because of the centrifugal force in the aorta curve, the secondary flow described above forms. The aorta is shown displaced to one side in order to make the flow visible.

2 Ventricle Model

2.1 Geometrical Model

The starting point of the dynamic geometry model of the moving inner wall of the left ventricle (Fig. 12) is two sets of MRT image data of the healthy human heart, taken at the University Hospitals of Bonn (Schiller (2002)) and Freiburg (Jung (2003)).

MRT Image Data

Eighteen horizontal sections are taken from the top of the heart, through the mitral valve, as well as 5 vertical sections through the middle of the left ventricle. The sections are rotated about different angles so that the ventricles are seen as fully as possible. In addition, three sections are taken perpendicular to the aortic valve plane. In fitting the boundary conditions of the simulation calculations and the validations of the simulation results, the blood flow in the heart is determined by means of the MRT phase contrast flow measurements. This must be carried out at the same number of cardiac cycles as the earlier

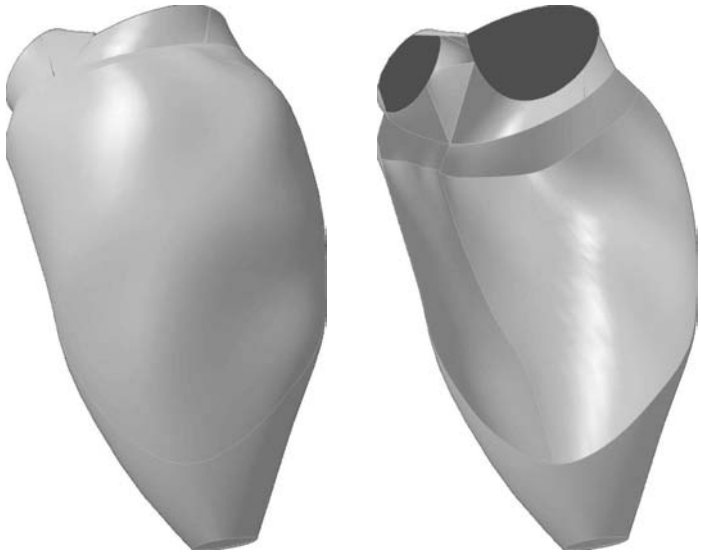

Fig. 12. Geometrical model of the left human ventricle

image data. The blood flow is measured perpendicular to the aortic valve and the mitral valve plane, as well as in the so-called three-chamber view of the left ventricle exit tract.

The problem in producing pictures of the heart is that the movement of the heart and the fast flow of blood make obtaining meaningful images difficult. The breathing of the patient is a further problem, as the motion of the diaphragm causes displacement of the heart in the chest. Therefore short exposure times and high resolution are necessary for taking images of the heart. Employing an electrocardiogram (ECG) and corresponding triggering of the image capture, new MRT data acquisition protocols make it possible to obtain time-resolved cine-records of the heart in a phase of only 15–20 seconds where the breath is held.

The time resolution of the image acquisition is 50 ms and is chosen depending on the frequency of the heart so that 17 cardiac cycles are recorded. The spatial resolution and thus the density of the individual layers is 6 mm.

The demands on the image acquisition and the MRT phase contrast flow measurements, as well as the optimization of the segmentation of the images is documented in the report by Schwarz (2003).

Segmentation of Images

In order to determine the dynamic geometry model of the left cardiac ventricle, the contours of the left myocardial wall in a cine-heart-MRT image of a healthy human heart are segmented, in all sections and in all cardiac cycles. The semi-automatic segmentation is carried out using the live-wire method of Mortensen and Barrett (1998). The segmentation method is based on the algorithm of Dijkstra (1959) to optimize the path search in a weighted graph.

Reconstruction of the Geometrical Model

Scatterplots are made from the segmented contour data for each time step, as shown in Figure 13. These are overlayed with a triangulation method in surface elements. Using a smoothing algorithm, the surfaces are interpolated and closed. The surface smoothing is controlled so that the ventricle volume is retained. The geometry model results from this, as shown in Figure 14 for a certain point in time. The entire view of the ventricle model is shown in Figure 11.

The opening and closing of the mitral and aortic flaps is pressure controlled. Figure 15 shows the systolic opening and closing process of the aortic valve with an image frequency of 50 Hz. The individual images are taken with the three-dimensional echocardiograph of Handke et al. (2003) and reconstructed three dimensionally, whereby the systole is covered with 50 images. The flap opening already reaches its maximum early in the systole. After this, closure begins, first taking place slowly and finally quickly. The systolic change of the shape of the opening surface is modelled in the projection onto the valve

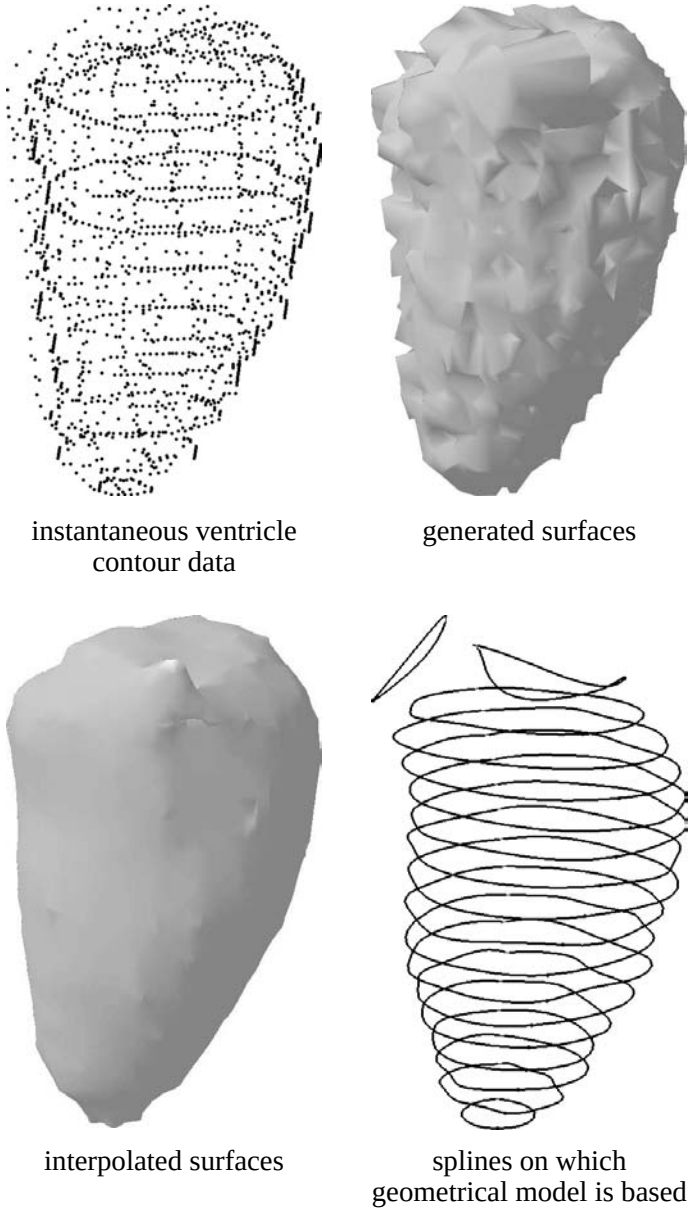

Fig. 13. Reconstruction of the geometrical model

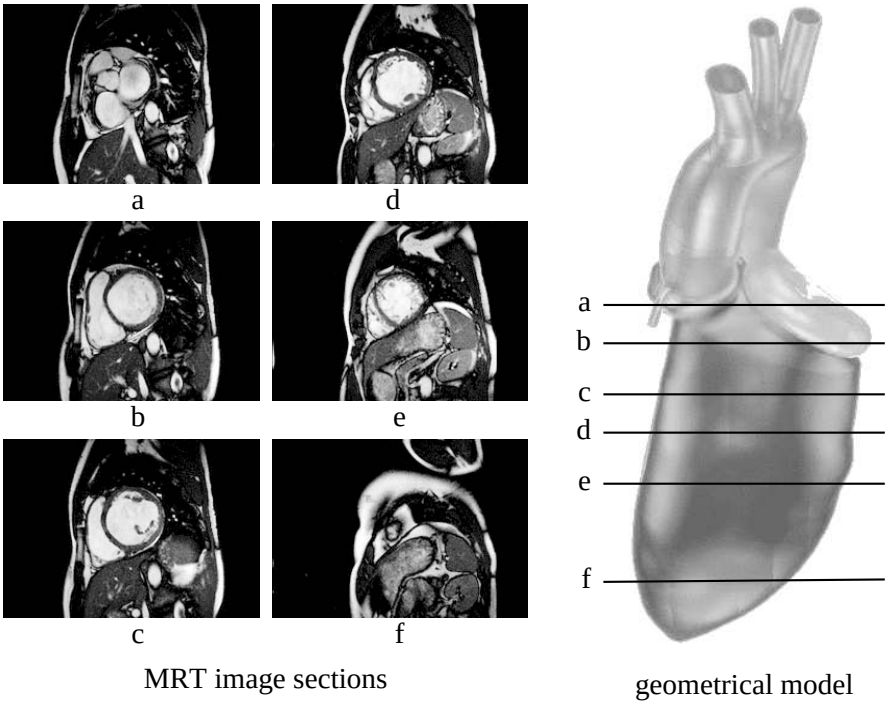

Fig. 14. MRT Image sections and geometrical model of the left human ventricle

plane.

Figure 16 shows the resulting two-dimensional model of the aortic and mitral valves. The volume fluxes determined with the MRT phase contrast flow measurement are modelled with the opening and closing projection surfaces of variable resistance. The mitral valve has two flaps which are mapped onto the projection plane with a variable slit diaphragm. The three crescent-shaped

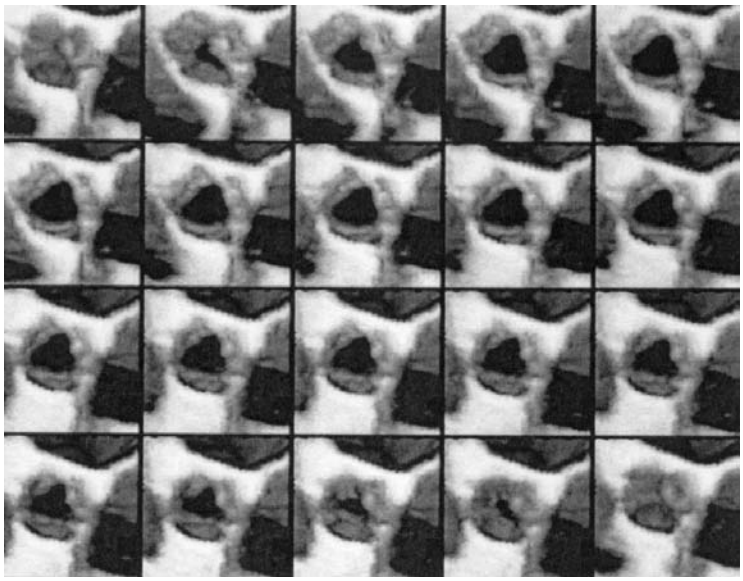

Fig. 15. Systolic opening and closure of the aortic valve, Handke et al. (2003)

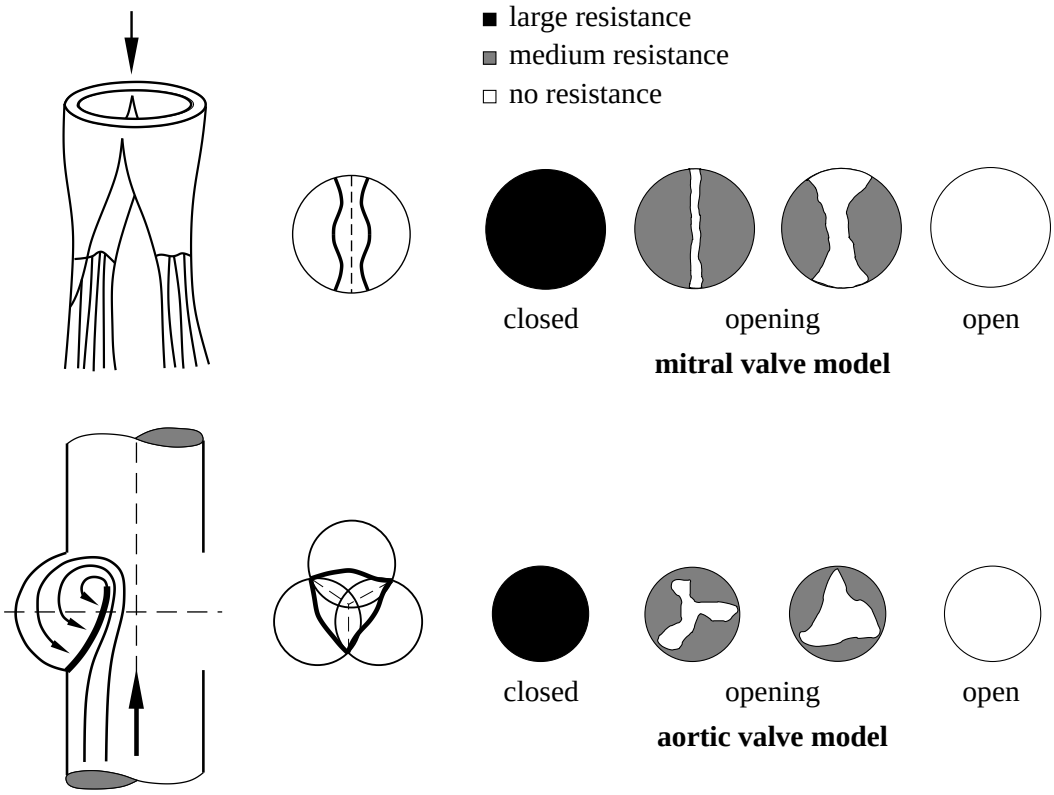

Fig. 16. Mitral and aortic valve model

connective tissue sacks of the aortic valve are simulated with a pin diaphragm of variable cross-section and resistance.

2.3 Numerical Model

The basis of the numerical model is the geometrical model of Figure 12. The flow in the left ventricle is determined by the motion of the geometrical model. The wake pressure p_{N}, forward pressure p_{V} and the circulation resistance K are shown in the circulation model in Figure 9. The pressure boundary conditions are formulated at sufficient distance from the cardiac valve model in Figure 16 to minimize the influence of the boundary conditions on the flow simulation in the ventricle. The numerical model of Figure 17 is expanded around a generic atrium and a generic aortic root, whose size is adapted to the mitral or aortic valve.

Computational Grid

The splines of the geometrical model of Figure 13 form the basis of the grid generation. The surface and the fluid space of the ventricle are covered with hexagonal cells, on top of which is placed an O-grid for the ventricle entry

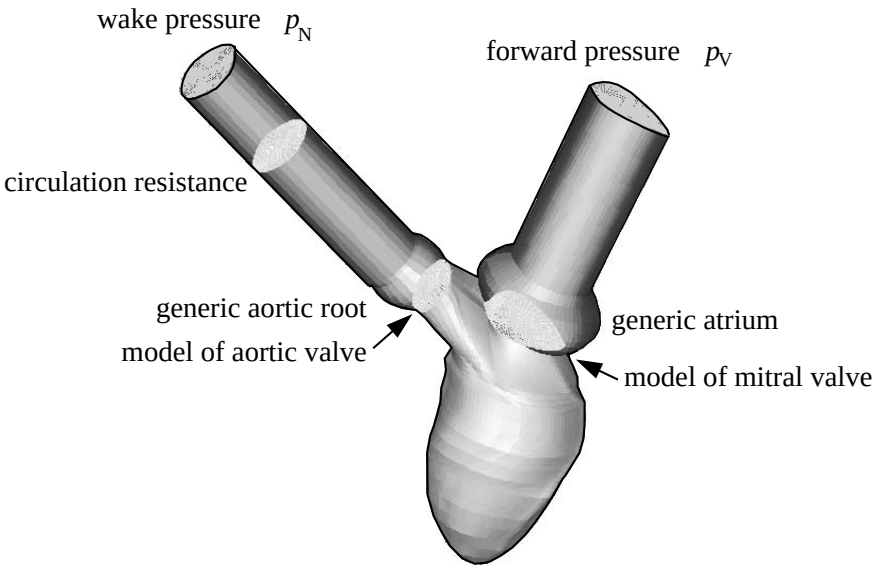

Fig. 17. Numerical model

and exit. The topology of the computational grid is shown in Figure 18. At every point in time at which MRT images exist, a separate grid is created. The resulting surface grid of Figure 19 is smoothed so that the ventricle volume is kept constant. The grids at each of the 18 points in time are generated so that they are topologically equivalent. The number of nodes and thus of cells is the same in all grids. The position of the nodes in the grid as well as their identity number also remains constant at each point in time. From the position of the node i at time t_n and at time t_{n+1}, intermediate grids are determined. Nonlinear interpolation is performed between the individual grids, so that it is ensured that the position vectors x_{n-1} and x_{n+1} pass continuously into each other.

The motion of the ventricle is different in different regions. The motion of the cardiac valve plane is little compared to the motion of the top of the heart. Therefore some sections of the grid, those that can be recognized clearly in

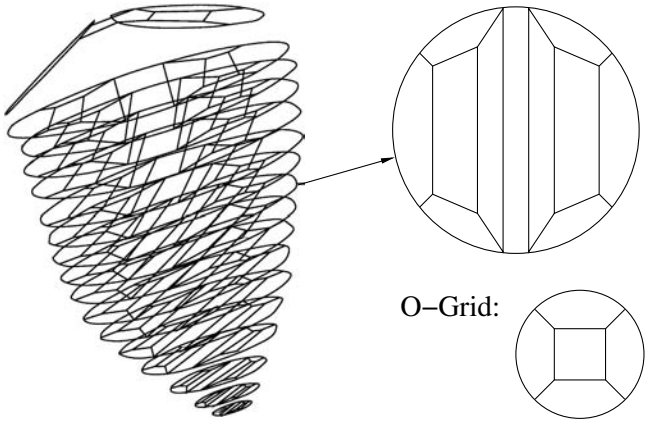

Fig. 18. Topology of the computational grid

the MRT images, are fixed. The remaining grid planes are distributed linearly between these. The global motion of the ventricle is therefore divided into regions of differently sized motion.

The flow structure in the ventricle to be calculated is dependent on the number of cells in the computational grid (see Oertel and Laurien (2003), Oertel et al. (2004)). Therefore first the grid dependence of the numerical solution in the ventricle described in the following section has to be analyzed. Figure 20 shows the projected streamlines in the central section of the ventricle during the systole and diastole for three different computational grids. The global flow structure has already been discussed in Figure 5. The intake vortex and its branching into the ventricle points during the diastole and the exit jet during the systole can be seen. The global flow structure is correctly given by all the computational grids shown, but there is some displacement of the foci in the central section of the ventricle. This is independent of the number of cells for a computational grid of more than 10^5 cells. With the selected time step size of $\Delta t = 9.5 \cdot 10^{-3}$, we obtain a Courant number of $Co = 8$. This is taken as a basis for the flow simulations in the following sections. For computational grids with more than $3 \cdot 10^5$ cells, there is deterioration in the rate of convergence, as both of the given grid topologies surround the cells at the entrance of the aorta too strongly.

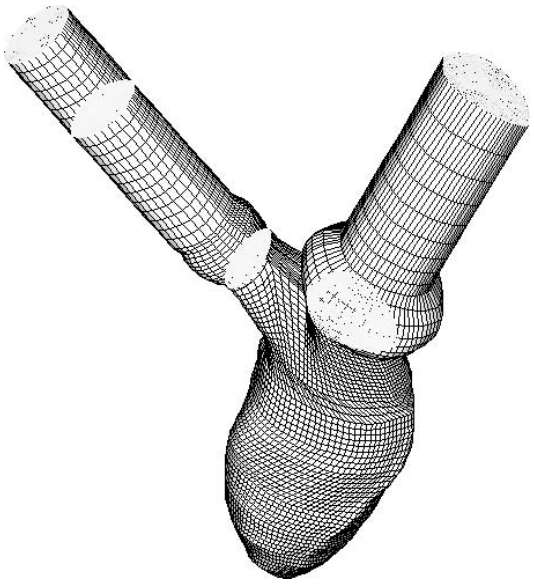

Fig. 19. Surface computational grid of the left ventricle

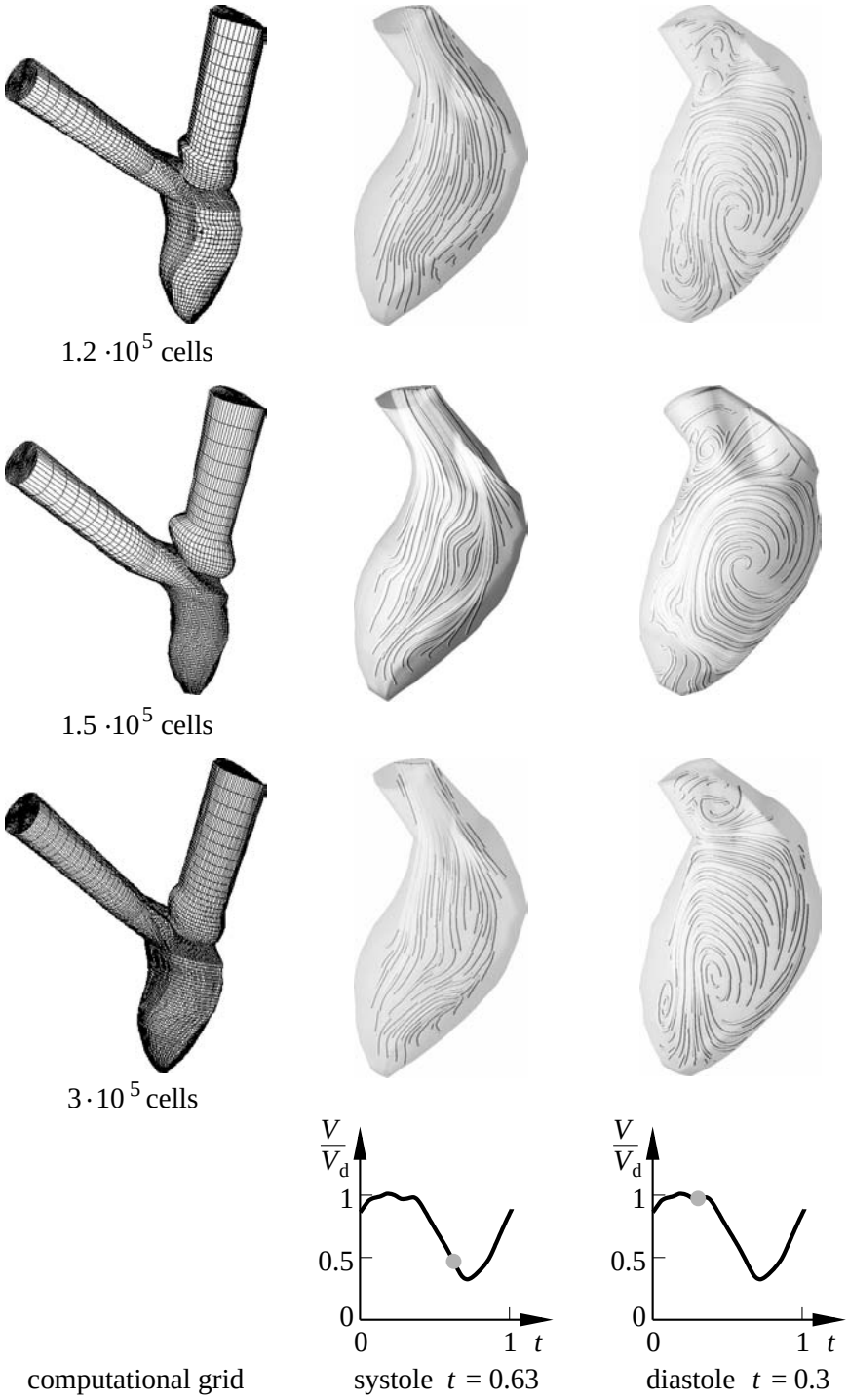

Fig. 20. Grid dependence of the flow structure in the left ventricle

For the calculation of the incompressible pulsating flow in the human left ventricle, the continuity and Navier-Stokes equations are made dimensionless with the characteristic diameter of the aorta D and the mean velocity U:

$$x^* = \frac{x}{D} \quad , \qquad v^* = \frac{v}{U} \quad , \qquad t^* = t \cdot \omega \quad , \qquad p^* = \frac{p}{\rho \cdot U^2} \quad .$$

Using the dimensionless characteristic Reynolds number $Re_D = U \cdot D/\nu_{\text{eff}}$, with $\nu_{\text{eff}} = \mu_{\text{eff}}/\rho$ from equation (5) and Womersley number $Wo = D \cdot \sqrt{\omega/\nu_{\text{eff}}}$ ($\omega = 2 \cdot \pi \cdot f$), we obtain the dimensionless equations:

$$\nabla \cdot v = 0 \quad , \tag{6}$$

$$\frac{Wo^2}{Re_D} \cdot \left(\frac{\partial v}{\partial t} + (v \cdot \nabla) v \right) = -\nabla p + \frac{1}{Re_D} \cdot \Delta v \quad . \tag{7}$$

The force tensor which acts on the flow from the inner walls of the heart is replaced by the movement of the geometrical model.

The numerical solution of equations (5) and (6) is carried out using the finite volume method and the numerical model of the previous section. The flow calculation is performed using the Star CD software package, Computational Dynamics Limited (2003). This software package has been verified for numerous applications in fluid mechanics, Oertel and Laurien (2003), Oertel (2004). The time discretization is performed with an implicit Euler method and the monotonic advection and reconstruction scheme. This second order method is carried out in two steps. First of all a field of monotonic gradients is defined, that together with the finite volume discretization guarantees a spatial second order discretization. In the second step the fluxes through the volume cell surface for all advectively transported quantities is reconstructed from the quantities calculated in the first step by means of a monotonic and bounded advection scheme. In order to calculate the incompressible blood flow, the PISO algorithm is applied. This introduces a further equation to calculate the pressure field. This PISO algorithm is a predictor-corrector method that calculates the temporally implicitly discretized unsteady flow. The details of the temporal and spatial discretization may be found in Oertel and Laurien (2003).

The results of the flow simulation are shown in Figures 22. The streamlines projected onto the plane of projection of Figure 21 are shown, together with the three-dimensional streamlines and velocity magnitudes of the left human ventricle. The anatomical and physiological parameters of the two healthy test

patients F1 and B1 are summarized in Table 1. For both patients, the same flow structure is found in the left ventricle as is denoted by the characteristics points of the flow field foci F and saddles S.

At the time $t = 0.76$ the mitral valve opens. At $t = 0.85$ the intake flow process in the ventricle is fully developed. At $t = 0.95$ the intake vortex forms in the empty part of the ventricle. This expands and branches up to $t = 0.25$. At $t = 0.25$ the intake flow process is complete, and the flow vortex is orientated to prepare for the exit flow through the aortic valve. At $t = 0.38$ the aortic valve opens and the exit flow into the aorta begins. At $t = 0.43$ the exit flow process is in full flow.

Shortly after the mitral valve opens, the streamlines in the upper part of the ventricle are arranged almost parallel and are directed towards the top of the ventricle. The fluid in the lower part of the ventricle has not yet been reached by the intake flow movement.

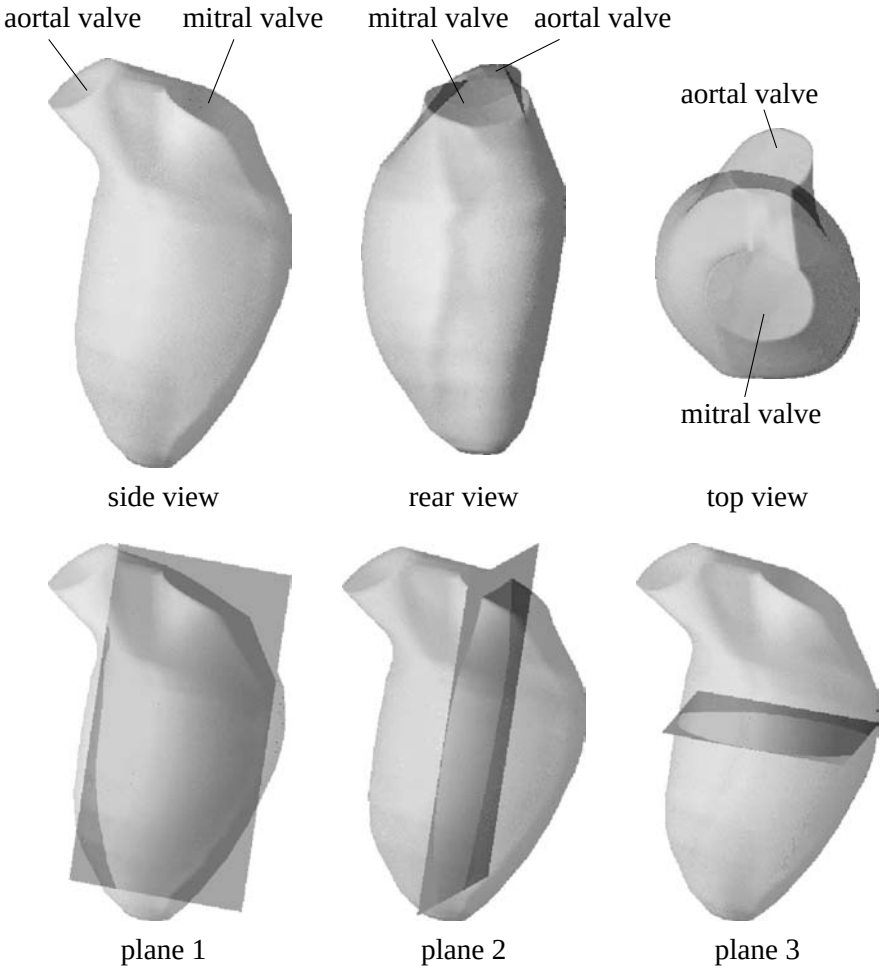

Fig. 21. Ventricle geometry and projection planes of the streamlines

The velocity maximum during the intake flow reaches the mitral valve surface (Fig. 23). After this, the intake process gives the streamlines their orientation in the whole ventricle. The fluid passes through the entire surface of the mitral valve with its maximum velocity. The blood flowing into the ventricle is slowed down by the blood at rest in the ventricle, and a ring vortex is formed in the upper part of the ventricle. The ring vortex has the shape of a torus and the fluid passes the surface of this torus along the shortest path. The direction of motion of the fluid can most easily be seen in sections through the torus. The reason for the formation of a ring vortex is that the velocity of the incoming blood in the upper part of the ventricle is larger than that in the lower part. The blood that is at rest in the ventricle is accelerated by the intake jet, but is unable to pass into the lower part of the ventricle. The ring vortex arises to balance this motion. As the diastole continues, the ring vortex increases in

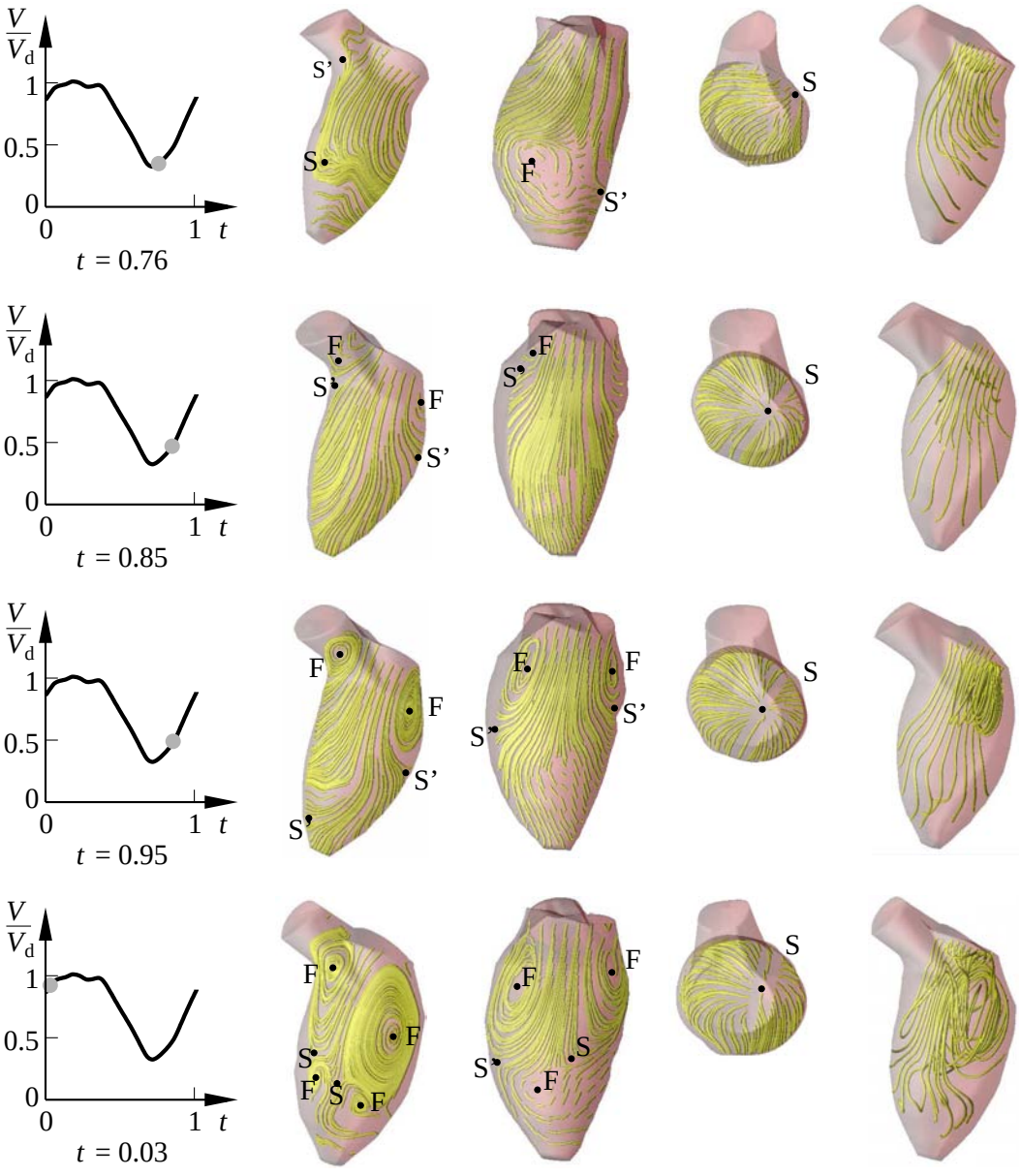

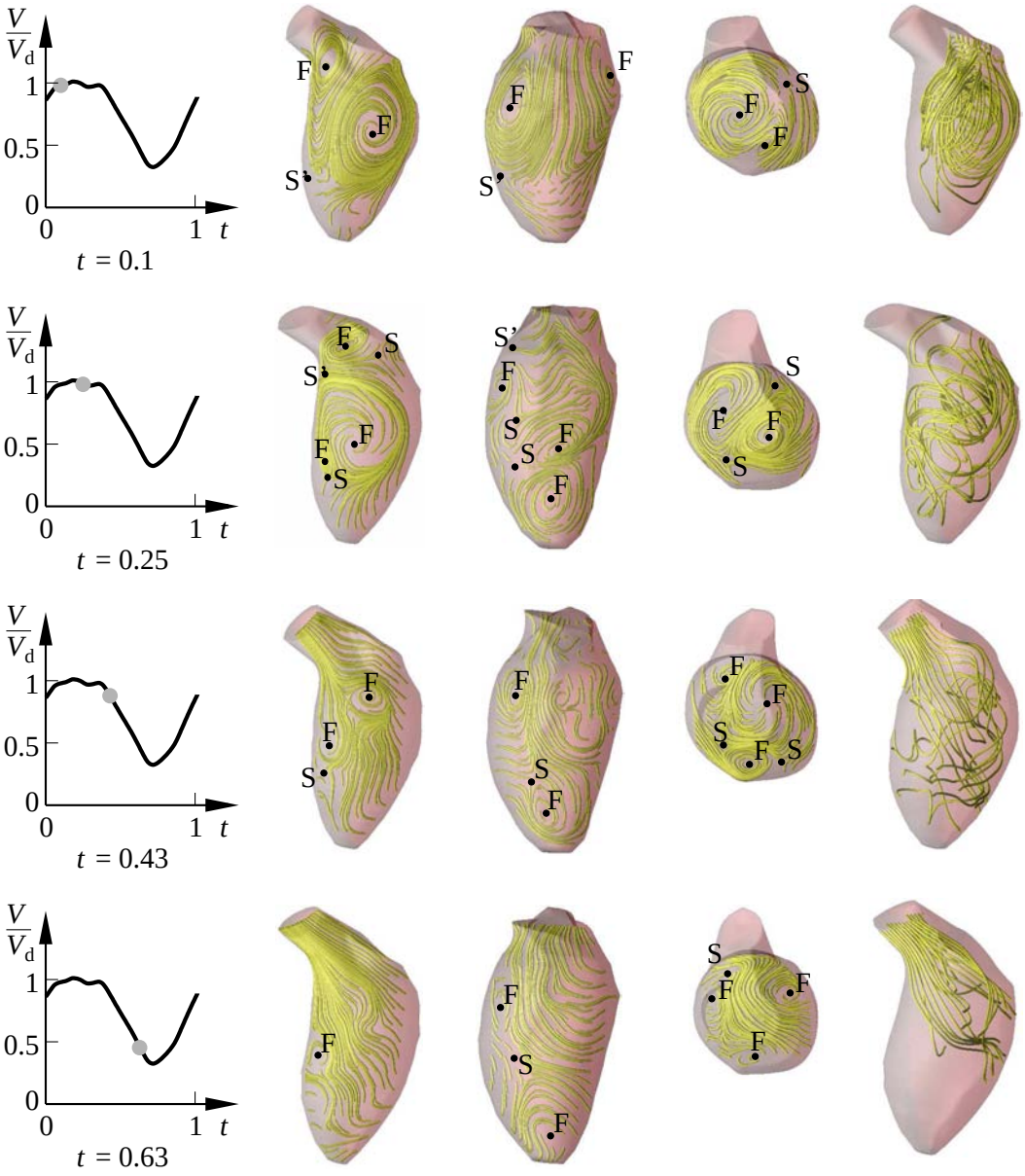

Fig. 22. Projected and three-dimensional streamlines in the left ventricle $Re_{D,\text{diastolic}} = 1079$, $Re_{D,\text{systolic}} = 2739$, $Wo = 25.2$, $T_0 = 0.77$ s

size. Its expansion in the axial direction is uniform, however the expansion in the radial direction is considerably greater on the right-hand side than on the left. The cause of this is the motion of the ventricle. During the diastole, the ventricle stretches more to the right than the the left, where it is connected to the right ventricle. Likewise, when viewed from behind, the expansion of the ring vortex is greater towards the left side than to the right, as the extension of the ventricle is greater in this direction. At the time $t = 0.03$ an additional small ring vortex can be seen. This arises because the fluid in the lower part of the ventricle gets an impulse from the upper larger ring vortex and thus is moved with it. Hence the smaller ring vortex rotating in the opposite direction

forms. However its velocity is very small. It has hardly any kinetic energy and is later dampened and dispersed. Throughout the rest of the diastole a further expansion of the ring vortex on the right-hand side can be seen, until finally there is only a small change in the volume of the ventricle. The intake process is then complete. The deformation of the vortex structure at this point in time is determined by the inertia of the vortex. The right part of the ring vortex moves towards the middle of the ventricle. Finally a branching of the ring vortex takes place and a new focus (F1) and a saddle point (S) are formed. If there were two foci until now, one on the left (F1) and one on the right side (F2), the strong deformation causes the left part of the ring vortex to divide into two foci, one upper (F1) and one lower (F3). The focus F1 moves off in the direction of the aortic valve.

Parameters	Data F1	Data B1
beat volume:	$8.51 \cdot 10^{-5}$ m^3	$7.51 \cdot 10^{-5}$ m^3
end diastolic volume V_{D}:	$14.01 \cdot 10^{-5}$ m^3	$15.1 \cdot 10^{-5}$ m^3
end systolic volume V_{S}:	$5.48 \cdot 10^{-5}$ m^3	$7.51 \cdot 10^{-5}$ m^3
pulse:	78 bpm	60 bpm
total cycle time T_0:	$0.77\,s$	$1\,s$
systolic time t_{S}:	0.3 s	0.39 s
diastolic time t_{D}:	0.47 s	0.61 s
mitral valve surface A_{M}:	$5.82 \cdot 10^{-4}$ m^2	$5.28 \cdot 10^{-4}$ m^2
aortic valve surface A_{A}:	$3.71 \cdot 10^{-4}$ m^2	$2.85 \cdot 10^{-4}$ m^2
forward pressure P_{V}:	500 Pa	500 Pa
blood pressure P_{B}:	$1.57 \cdot 10^4$ Pa	$1.60 \cdot 10^4$ Pa
mean velocity (diastole) v_{dia}:	0.31 m/s	0.23 m/s
mean velocity (systole) v_{sys}:	0.76 m/s	0.68 m/s
mean viscosity $\overline{\mu_{\mathrm{eff}}}$:	0.0061 kg/ms	0.0082 kg/ms
density ρ:	1008 kg/m^3	1008 kg/m^3
Re_{D} (systolic):	2739	1579
Re_{D} (diastolic):	1079	739
Wo (systolic):	31.4	13.7
Wo (diastolic):	25.2	10.9

Table 1. Anatomical and physiological parameters of the flow simulation in the ventricle

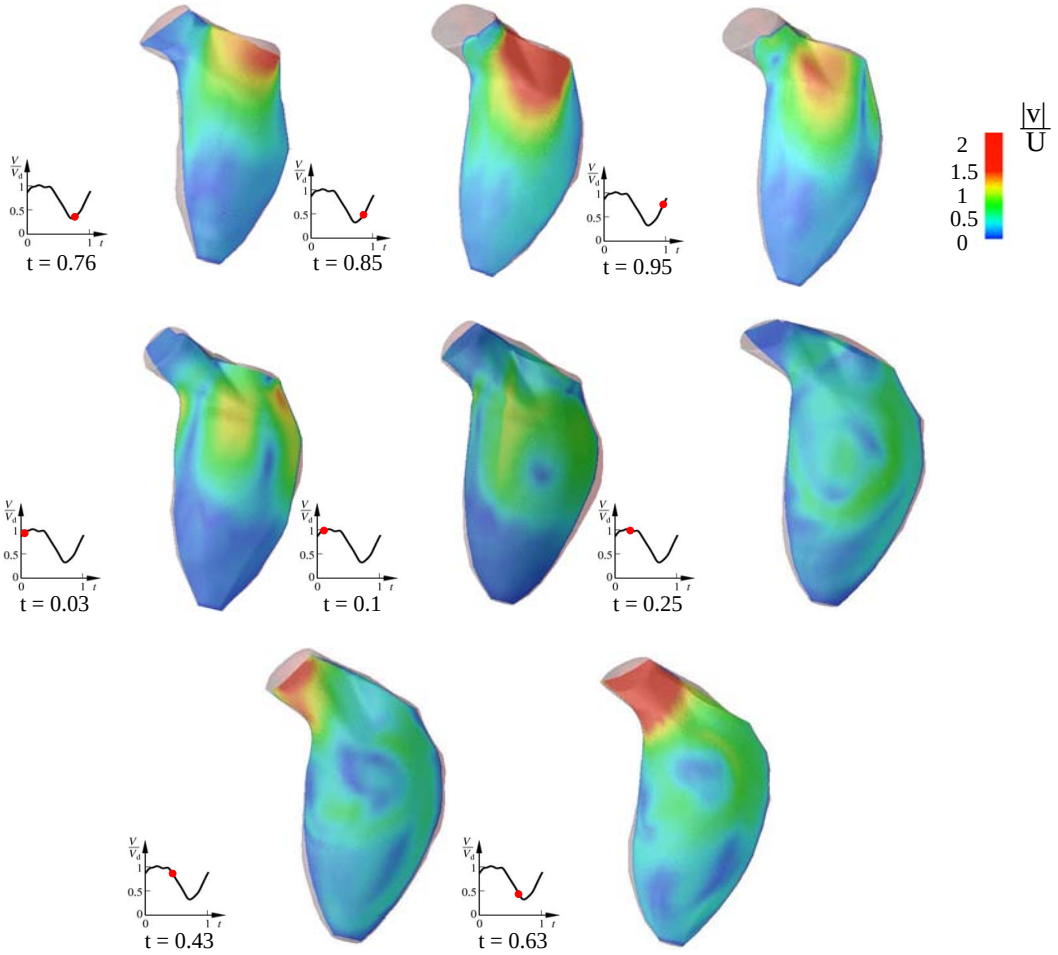

Fig. 23. Velocity magnitudes in the left ventricle $Re_{D,\text{diastolic}} = 1079$, $Re_{D,\text{systolic}} = 2739$, $Wo = 25.2$, $T_0 = 0.77$ s

At the beginning of the systole, the fluid begins to pass out of the ventricle as the aortic valve begins its opening phase. The ring vortex thus keeps moving in the same direction. The focus F1 of the left part of the vortex is already washed out at the time $t = 0.43$ and it pulls the right focus F2 after it. The left focus F3 has increased in size. The velocity maximum of the exit flow process is reached in the central region of the aortic valve surface and a jet flow forms in the aorta. At $t = 0.63$ the exit flow is fully developed. The vortex structure is still partially in place and will only completely dissipate at the end of the systole. The blood now flows through the entire aortic valve surface with its maximum velocity.

2.5 Validation

The validation of the flow simulation in the left human ventricle is carried out with MRT phase contrast flux measurement (Schiller (2002)).

In validating the flow structure, the results of the MRT phase contrast flux measurement are compared with the results for the the flow simulation. The measurement of the flux data is carried out in the same plane as the MRT data images that are the basis for the geometrical model of the flow simulation. Thus segmented contours of the ventricle from the MRT images can be carried over to the images of the flow (Fig. 24). Comparison between the isotachic lines evaluated from the flux measurements and those from the flow simulation is shown in Figure 25. The regions of equivalent directions of the velocity are in agreement, both in their position and in their size. Thus the global flow structure in the left ventricle of Figure 5 is validated.

2.6 Model Prediction

The evaluation of the results of the flow simulation in the left human ventricle leads to the sketched flow structure in Figure 26. The summarizing figure of the flow development in the ventricle throughout one cardiac cycle is shown in Figure 5. The stroke volume of a healthy human ventricle compared to the average measurements over many hearts is shown in Figure 27 (Fung (1997)). The mean value of the stroke volume is in agreement. However the filling of the ventricle top begins at different times. The measured and calculated mean maximal pressure in the ventricle is $1.6 \cdot 10^4$ Pa, corresponding to the value 160 bar in Figure 3.

From the simulation results, the p–V diagram of the ventricle is evaluated for the data of F1 in Table 1. Figure 28 shows the result. The stroke work of the healthy human heart is calculated to be 0.78 J.

With the flow simulations in the healthy human ventricle, the foundations have been laid to analyze pathological cases of ventricle defects and to make predictions on the flow losses in unhealthy human hearts using the KAHMO heart model. We will return to this in the final chapter.

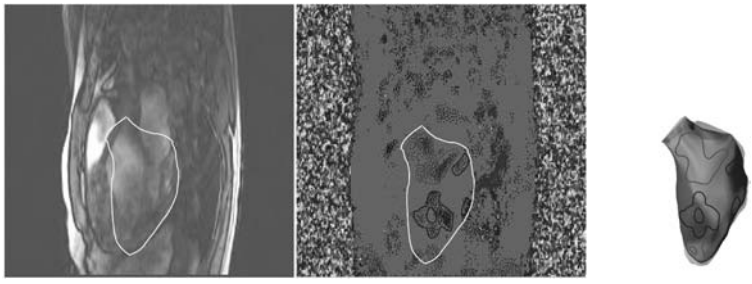

Fig. 24. Rendering of the MRT flux measurement onto the simulation results

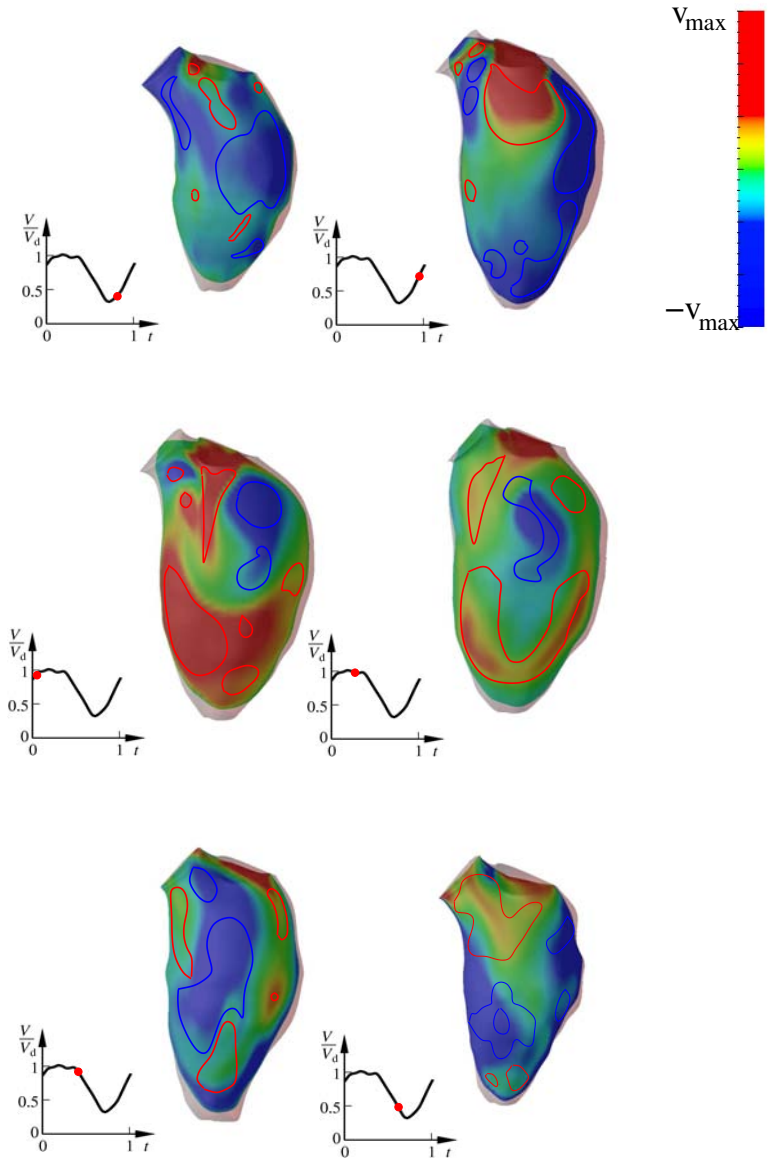

Fig. 25. Comparison of the isotachic lines from the MRT flow measurement and the simulation results

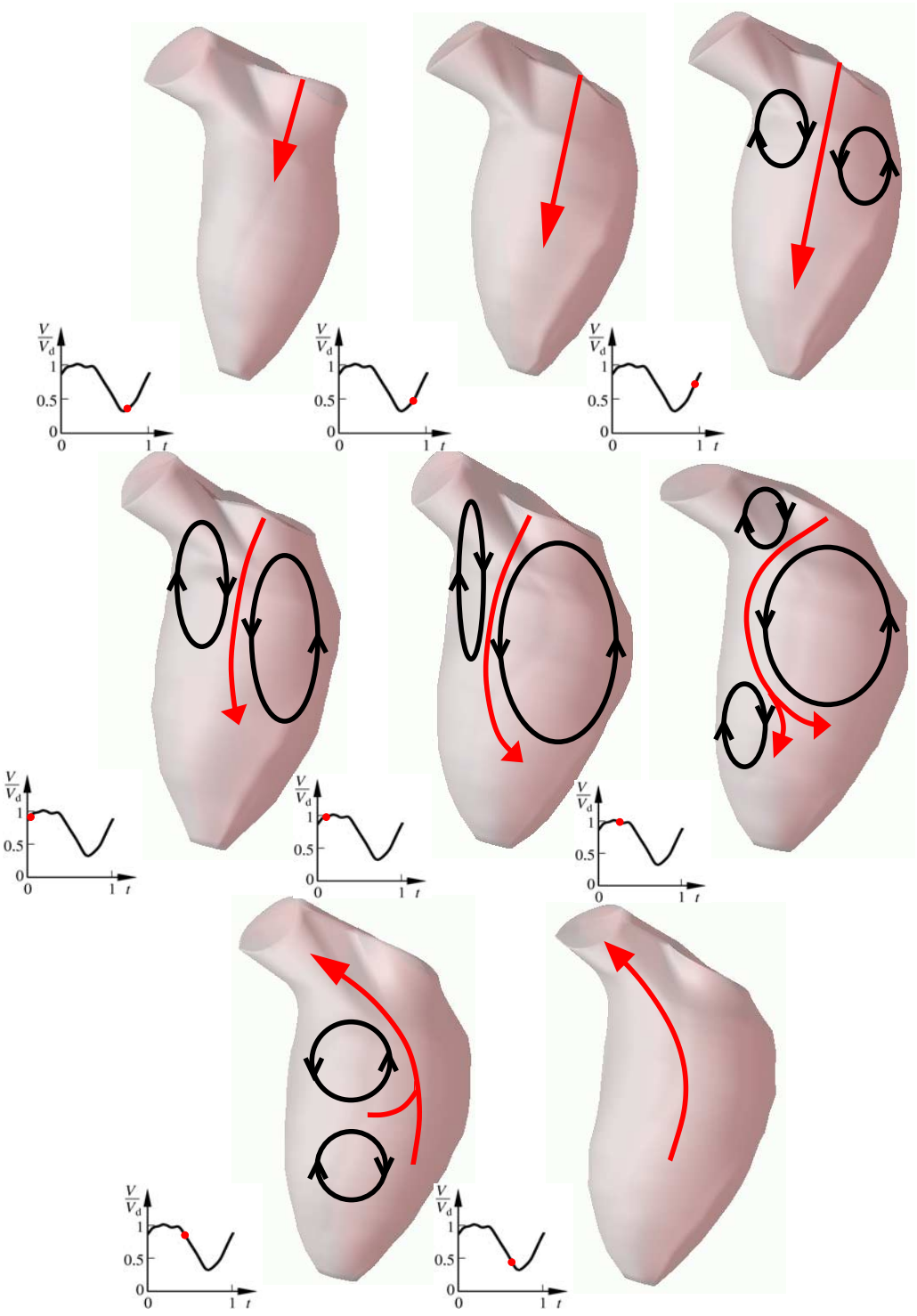

Fig. 26. Flow structure in the left ventricle $Re_{D,\text{diastolic}} = 1079$, $Re_{D,\text{systolic}} = 2739$, $Wo = 25.2$, $T_0 = 0.77$ s

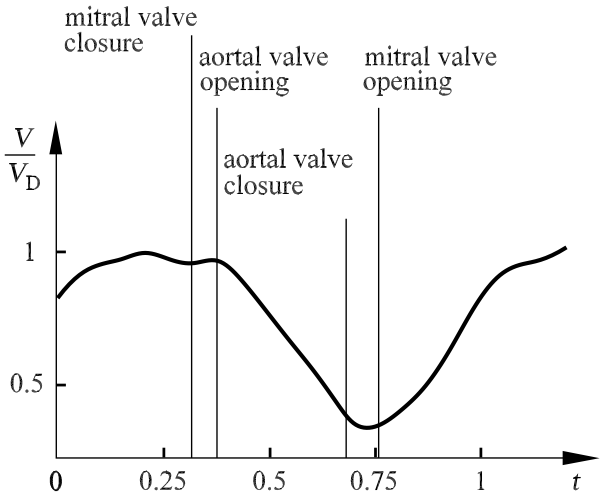

Fig. 27. Stroke volume of the left ventricle $V_{\mathrm{D}} = 1.4 \cdot 10^{-4}$ m^3, $T_0 = 0.77$ s

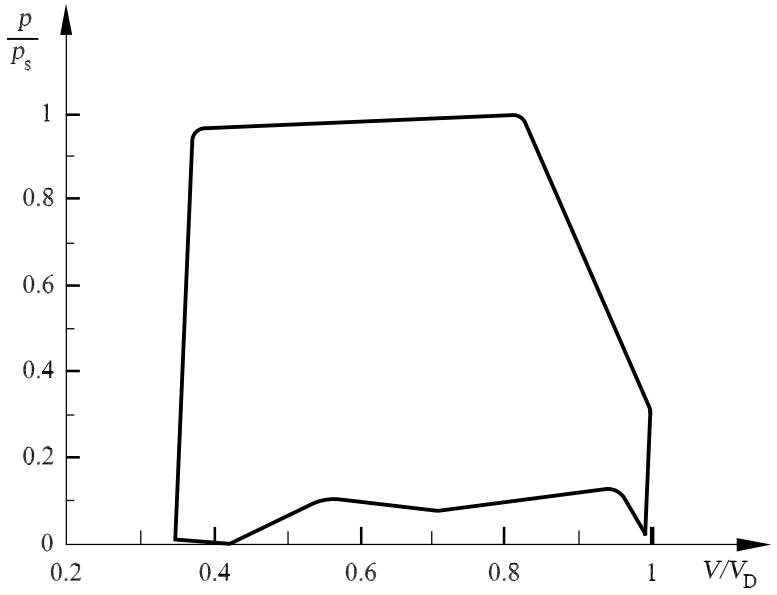

Fig. 28. p–V diagram of the left ventricle $Re_{D,\mathrm{diastolic}} = 1079$, $Re_{D,\mathrm{systolic}} = 2739$, $p_{\mathrm{S}} = 1.5 \cdot 10^4$ Pa, $V_{\mathrm{D}} = 1.4 \cdot 10^{-4}$ m^3, $Wo = 25.2$, $T_0 = 0.77$ s

3 Aorta Model

In order to calculate the model aorta that forms the inactive part of the left KAHMO heart model, a flow-structure coupling is necessary. The pulsing blood flow of the left ventricle causes a deviation of the aorta that is accompanied by an increase in volume. Therefore the motion cannot be predicted for the flow calculation, but rather must be determined via a structure calculation. The model aorta is to approximate the natural aorta as closely as possible with respect to its elastic properties. The assumption of a model aorta is justified, as in general no MRT images of the aorta are taken in clinical investigation of the human heart.

The model aorta was generated by discharge of an aorta specimen by Liepsch et al. (1992). The aorta is that of a young woman without pathological conditions. In order to attain good fine structure accuracy, the discharge was carried out post mortem. Different levels of molding led to a build-up of silicon in the aorta specimen, corresponding to the elastic properties of the human aorta.

3.1 Geometrical Model

The geometrical model of the silicon specimen of the model aorta is shown in Figure 29. It consists of the ascending and descending aorta as well as the exits

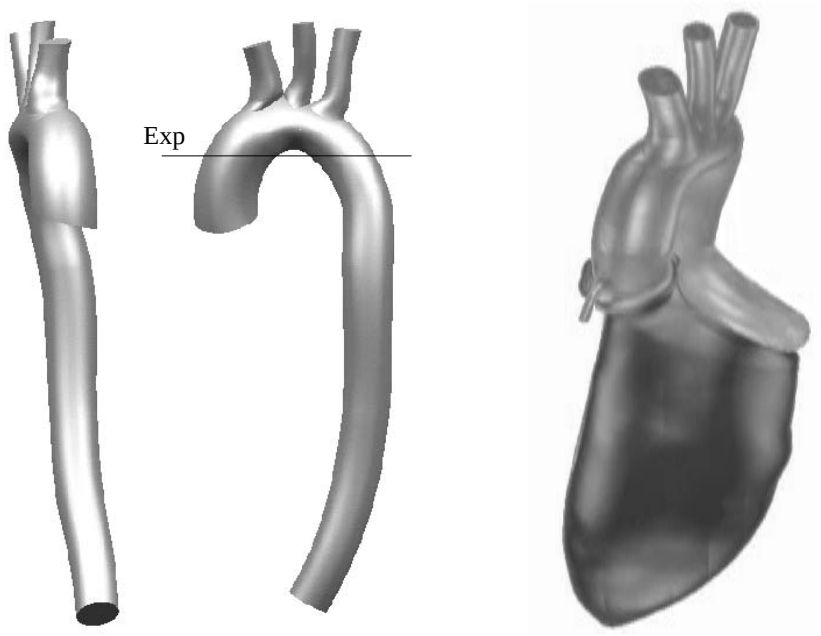

Fig. 29. Geometrical model of the aorta and its connection to the left ventricle

to the collar bone and neck arteries in the bend in the aorta. The connection to the left ventricle is via a flexible generic aortic root that models the transition upstream of the aortic valve.

3.2 Flow-Structure Coupling

To calculate the structure of the aorta, a first linear approach is made using the software package Permas (INTES (2000)). The software package is based on the finite element method. The spatial discretization is carried out using form functions that are weighted with the functional values in the elementary nodes. The stress-tension properties of the aorta are taken from the literature. The flow-structure coupling is partitioned. The flow and structure fields of the aorta are calculated separately and suitable load quantities such as the pressure and the shear stress components are compared after every time step. The transfer of the shear stress tensor of the flow calculation onto the nodes of the structure program is performed using the coupling library MpCCI, Fraunhofer Institute for Algorithms and Scientific Computing (2000). An important condition for successful coupling of the different computational grids of the flow and structure calculation (Fig. 30) is an efficient algorithm to automatically search for neighborhoods in the computational grids. To this end a Bucket algorithm is employed.

The disadvantage of the weakly partitioned coupling of the flow calculation with the linear structure calculation is the fact that no equilibrium position can be calculated. As it is only the calculation of the volume reservoir of the aorta integrated into the circulation model and the flow drag that are of interest within the framework of the KAHMO heart model, the selected coupling model is sufficient. However, if we are interested in the details of the coupling mechanism, a more strongly nonlinear and iterative coupling

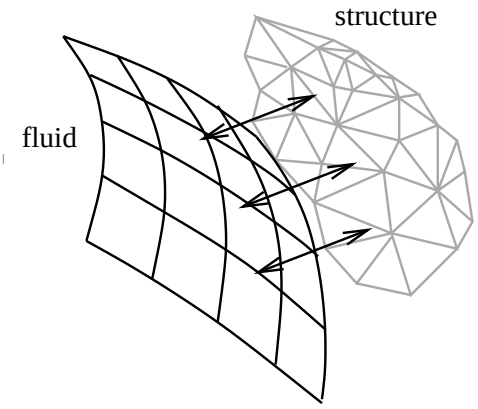

Fig. 30. Exchange of flow and structure quantities with the coupling library MpCCI, Fraunhofer Institute for Algorithms and Scientific Computing (2000)

algorithm must be selected.

3.3 Numerical Model

The numerical model to calculate the flow in the model aorta is shown in Figure 31. At the intake edge of the ascending aorta, the velocity distribution of the ventricle calculation is given. At the exit edge of the branching and descending aorta, each of the pressures and circulation resistances calculated with the circulation model are given. Using the pressure given by the boundary conditions, the stress-free exit geometry of the model aorta is prescribed.

Generation of the computational grids and the demonstration of the grid independence of the simulation results is carried out in the same way as in Section 2.3.

3.4 Validation

Validation of the flow-structure coupling model is carried out using the silicon aorta specimen (Liepsch et al. (1992)). The silicon has isotropic material properties with E–modulus $E = 1.9 \cdot 10^6$ N/m^2, transverse contraction number $r = 0.49$, density $\rho_s = 970$ kg/m^3 and refractive index $n = 1.413$, corresponding to the transparent model fluid. It is known from expansion measurements

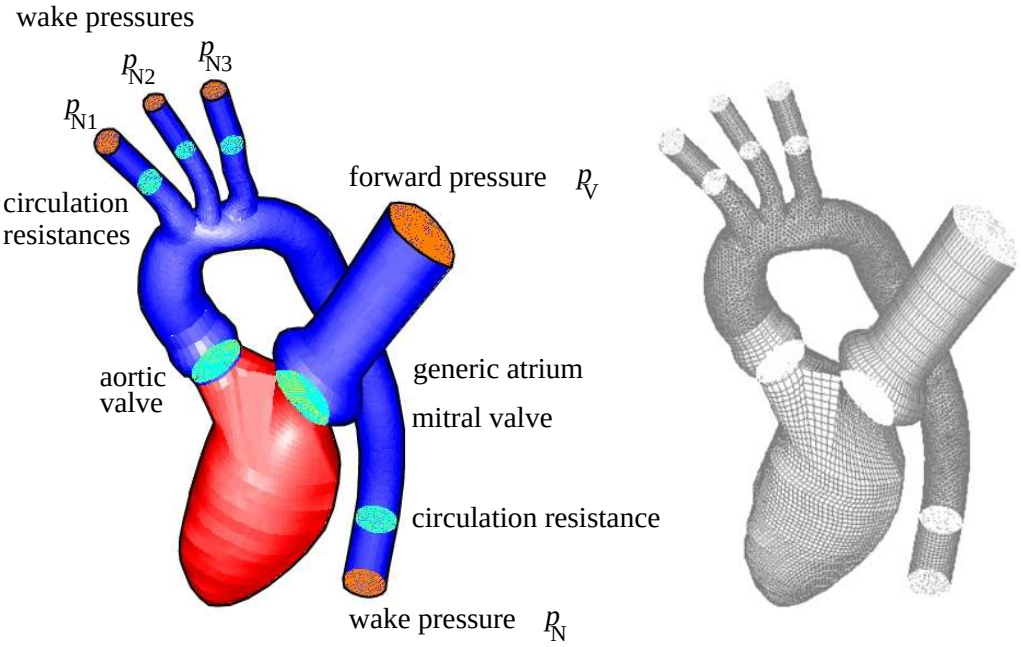

Fig. 31. Numerical model and surface grid

that the aorta specimen can be approximated with a linear constitutive relation.

The measurement of the local velocities in selected sections of the model aorta is carried out using laser-Doppler anemometry (LDA). The pulsing flow in the aorta specimen is given by the model ventricle of Section 2.5 with the cardiac cycle $T_0 = 0.77$ s and Wormersley number $Wo = 25.2$. The diameter of the ascending aorta is $D = 2.2 \cdot 10^{-2}$ m. With the viscosity of the model fluid $\mu = 3.18 \cdot 10^{-3}$ p and the volume flux $\dot{V} = 226$ l/h, the Reynolds number is therefore $Re_D = 1350$.

The same parameters are chosen for the numerical flow simulation of the elastic aortic bend as in the experiment.

The wall strength distribution of the aortic model is matched to the wall strength of the aortic specimen in experiment (Fig. 32). In the experiment the aortic specimen is attached at it entrances and exits with plexiglas tubes. For the structure-mechanical calculation this means that the freedom of motion at these edges is restricted. Therefore, just as with the structure calculation at the edges, all degrees of freedom are suppressed.

Comparison of the flow calculation with the model aorta and the experiment in the aorta specimen shows good agreement during the systole. Differences

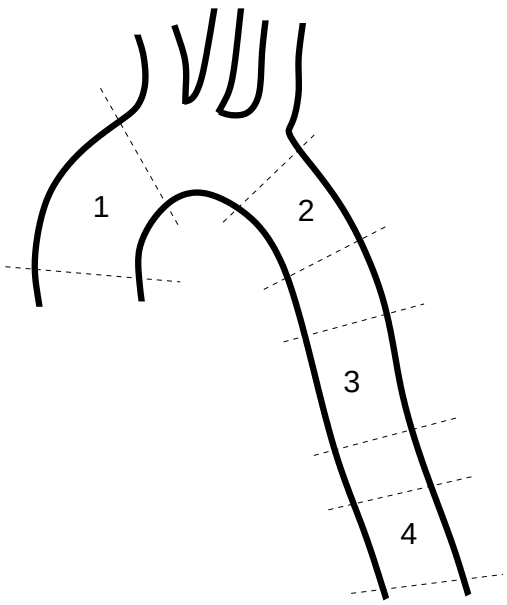

Section I	Section II	Section III	Section IV
14.7	14.3	11.3	9.7

radius – wall thickness conditions r/h

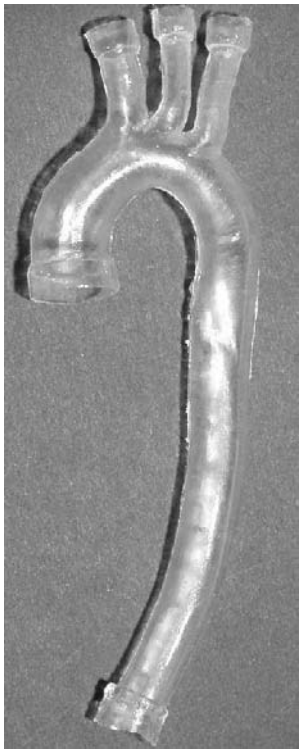

Fig. 32. Segments of the aortic specimen and the wall strength distribution

Parameters	Section 1	Section 2	Section 3	Section 4
r/h	36	34	25	23
E–modulus $N/m^2 \cdot 10^6$	1.2	1.19	1.16	1.26

Table 2. Wall thickness and material properties of the aorta sections

between the measurement and the simulation calculation appear at the start of the diastole as the flow slows down in the ascending and descending aorta. In the experiment there is a uniformly small backflow in the ascending aorta. At the same point in time, the velocity in the simulation calculation sinks to a minimum, although it is still positive. This may be due to the different formulation of the circulation and boundary conditions. The deviation and the volume change of the model aorta is correctly given by the simulation results with the simplified linear flow structure coupling, so that the aim of the validation is attained, namely the calculation of the flow losses and pressure boundary conditions of the aorta in the circulation model.

3.5 Model Predictions

With the validated flow-structure coupling of the inactive part of the KAHMO heart model, simulation calculations with the left ventricle and the flow parameters F1 of Table 1 as well as with the model aorta of Figure 29 are carried out. In contrast to the aortic specimen of the validation experiment, now the stress-tension model and the wall strength distributions of the human aorta are used. To do this the sectional division of Figure 32 is used.

Figure 34 shows the calculated three-dimensional streamlines, the streamlines projected onto the longitudinal section and the velocity contributions during the systole on the basis of the ventricle velocity profile of Figure 33. At the beginning of the systole the flow in the model aorta quickly reaches its maximum and already exhibits a considerable deformation at $t = 0.43$. As expected from Figure 7, the flow profiles have a maximum at the inner side of the aortic bend. After passing through the entire curved region, the maximum shifts to the outer side of the aortic bend. The streamlines at the time $t = 0.43$ already indicate the secondary flow in the aortic bend. At time $t = 0.63$, the point of maximum deceleration of the flow occurs. The velocity profiles flatten and the streamlines indicate a first backflow in the ascending branch of the aorta. At time $t = 0.85$, the aorta has almost completely returned to its initial position.

In the ascending model aorta, a strong deviation due to the pressure pulse is observed. It is to be noted that the bulging deformation of the aorta in this region is caused by the close structure boundary condition at the aortic root. During the systole, because of the centrifugal force, the secondary flow forms

two vortices with two half-saddles. This structure is retained into the diastole. In spite of the deceleration of the flow that has already begun, the compliance of the aorta clearly contributes to a stabilization of the flow structure. At time $t = 0.85$ the structure finally breaks up. The main flow velocities are close to zero and the deformation of the aorta is again the same as its initial condition.

At the start of the systole there is still no evident secondary flow, and it is only at $t = 0.43$ that the first structures of the secondary flow can be seen. At time $t = 0.63$ the radial deviation motion of the aorta as already described can be observed. For a short time a triple-vortex configuration appears, only to decay again to the stable double vortex at $t = 0.67$. This double vortex structure of Figure 7 remains for the rest of the cardiac cycle.

In order to evaluate damage to the aorta wall caused by disease, a discussion of the wall shear stress is necessary, as shown in Figure 35 during the systole. At each of the opposite artery walls of the aortic branching, a maximum of the wall shear stress occurs during the systole. The velocity maximum at the inner side of the aortic bend at the start of the systole also leads to a maximum of the wall shear stress. If the wall shear stress is zero, temporary flow losses

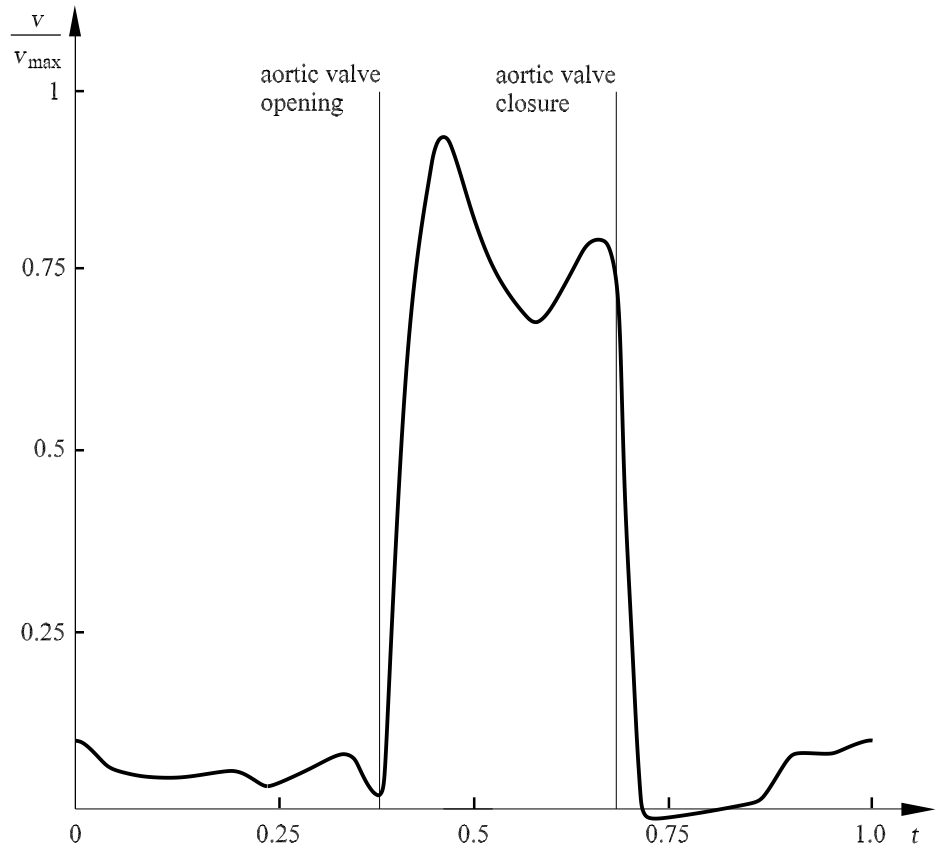

Fig. 33. Velocity distributions at the entrance to the model aorta, $Re_{D,\text{diastolic}} = 1079$, $Re_{D,\text{systolic}} = 2739$, $Wo = 25.2$, $T_0 = 0.77$ s

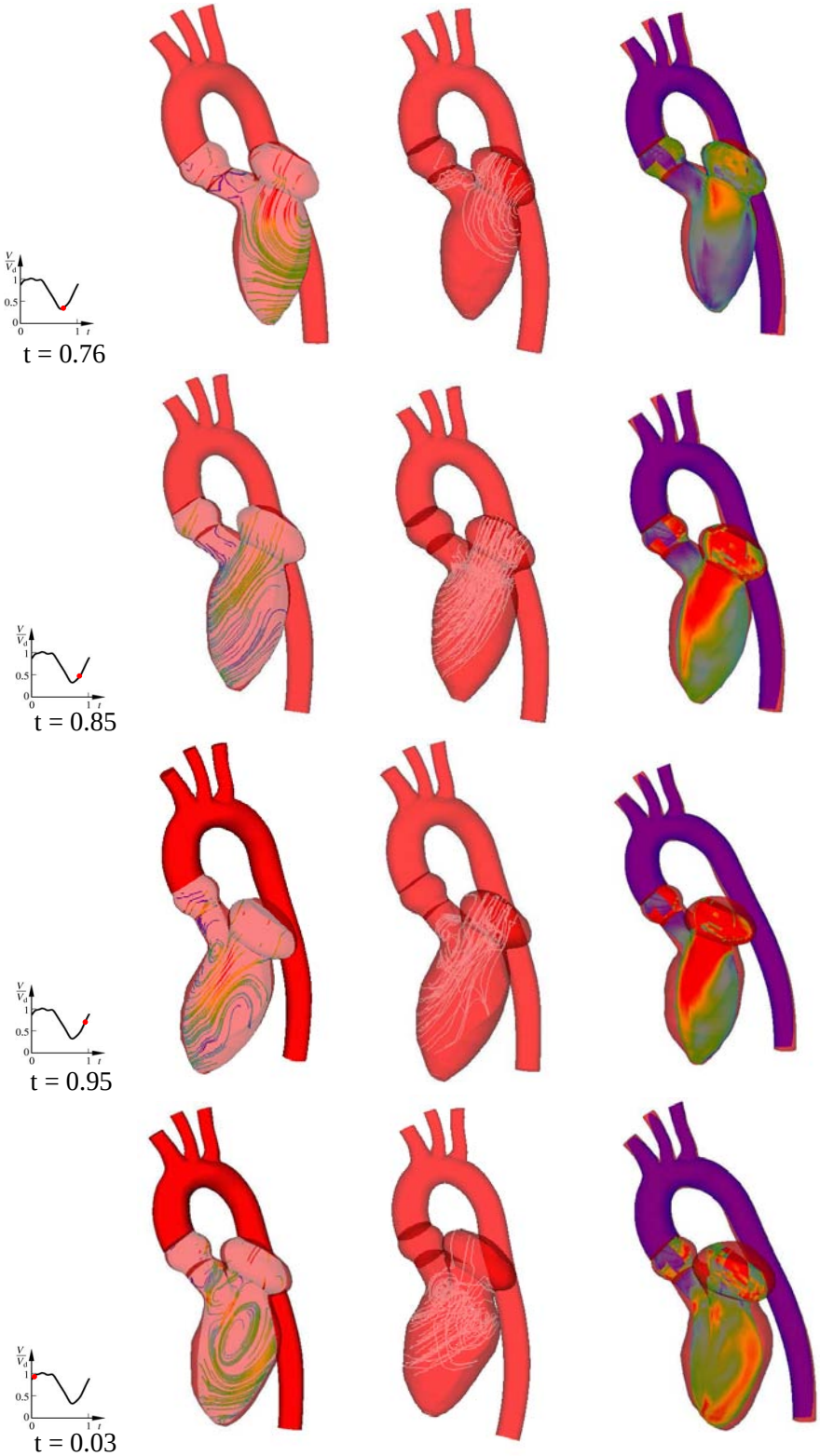
t = 0.76
t = 0.85
t = 0.95
t = 0.03
projected stream lines
stream lines
velocities

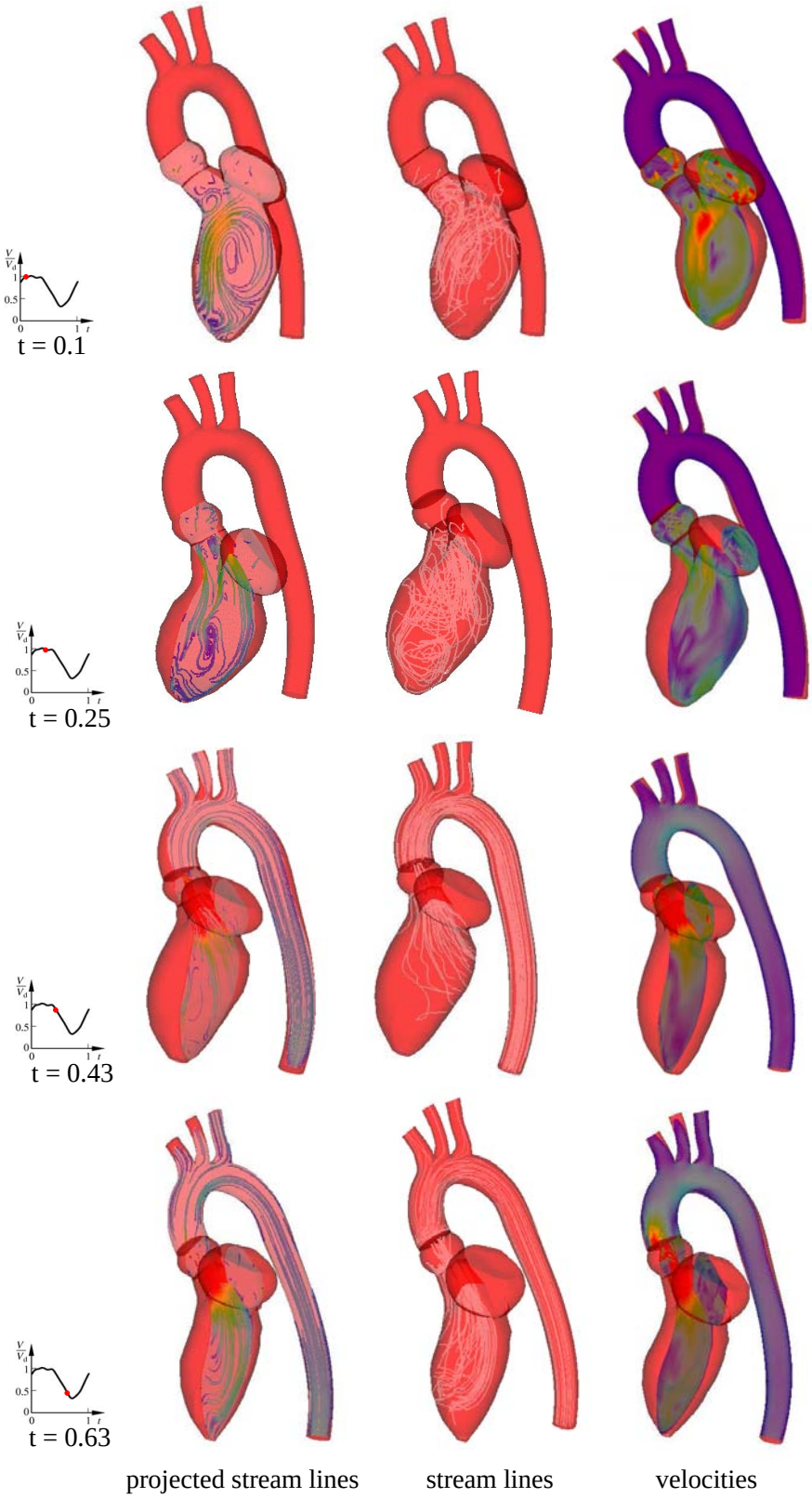

Fig. 34. Flow quantities in the human left ventricle and the model aorta $Re_{D,\text{diastolic}} = 1079$, $Re_{D,\text{systolic}} = 2739$, $Wo = 25.2$, $T_0 = 0.77$ s

Fig. 35. Aortic wall shear stress $Re_{D,\text{diastolic}} = 1079$, $Re_{D,\text{systolic}} = 2739$, $Wo = 25.2$, $T_0 = 0.77$ s

occur.

4 Discussion

4.1 Model Conclusions

With the validated KAHMO heart model, the flow quantities and flow structure in the healthy human heart based on MRT image data can be calculated. This forms a basis for the analysis of pathological cases of ventricle defects in human hearts (Schenkel et al. (2004)). In the case of *akinesia* of the left ventricle, the contraction amplitude is no longer present. *Dyskinesia* denotes a systolic outward motion of a myocardial area ,while an *aneurism* describes a large dyskinetic area with paradoxical pulsation or large akinetic outward sagging which is considerably larger than the normal wall contour even in the diastole. Figure 36 shows the fluid space of a healthy human ventricle, as well as two pathological cases. As the dyskinesia and the akinesia represent characteristic pathological cases and can be modelled with an alteration in the volume flux of the KAHMO heart model, they have been selected for numerical flow simulation.

Just as in the case of a healthy human heart, during the systole in the presence of a dyskinesia of the left ventricle the intake vortex forms. However, the projected streamlines in the central section of the ventricle in Figure 37 show

that the vortex does not attain the same dominance on the left side of ventricle as in a healthy human ventricle. The bulging changes the configuration so that it forms a natural obstacle for the vortex. As a consequence of the smaller left-side formation, the right vortex increases in size and forms an obstacle in front of the aortic valve. This behavior explains why the flow at the end of the intake flow process is not yet oriented in the direction of the aortic valve. Furthermore, the bulging region forms a volume reservoir where the blood collects and remains in the ventricle, even after several cardiac cycles.

At the beginning of the systole the flow does not have the geometric configuration of the healthy ventricle, leading to a deviating movement of the flow. The natural timing of the flow is lost. The flow then forms the same configuration as described for the healthy ventricle. However, the difference lies in the collecting function of the bulge that causes the blood to remain in the ventricle.

For an aneurism too, at the start of the intake process a ring vortex flows, whereby the left-side deviation of the myocardium prevents the dominance of the left-hand vortex over that on the right. In the entire lower region of the ventricle blood can collect and again remain for several cycles. At the start of the exit flow process it can be seen that a vortex remains against the wall on the right-hand side of the ventricle, keeping the blood in the lower part of the ventricle. The timing of the flow is sensitively disturbed, and numerical simulations show that the large quantity of remaining blood means that an aneurism is the worst pathological ventricle defect.

With respect to the flow structure, the modelled pathological ventricle defects show differences to the healthy ventricle such that complete functionality of the ventricle for a cardiac insufficiency is not longer present. The global flow structure in the ventricle is determined by the onset, expansion, branching and movement of the ring vortex.

The flow structure in a healthy ventricle is characterized by a ring vortex. The fluid flows along this ring vortex during the diastole. When the left vortex part splits off, the flow branches. The ventricle is emptied by contraction. As the

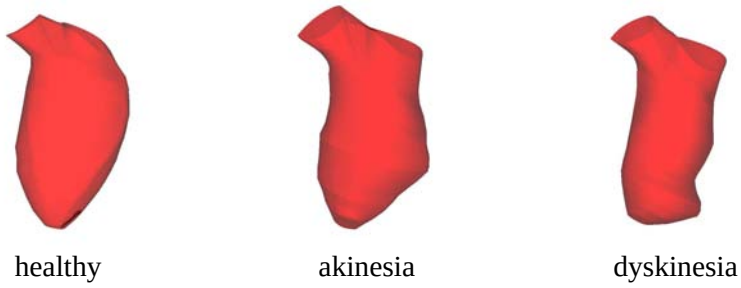

Fig. 36. Pathological ventricle defects of an akinesia and a dyskinesia

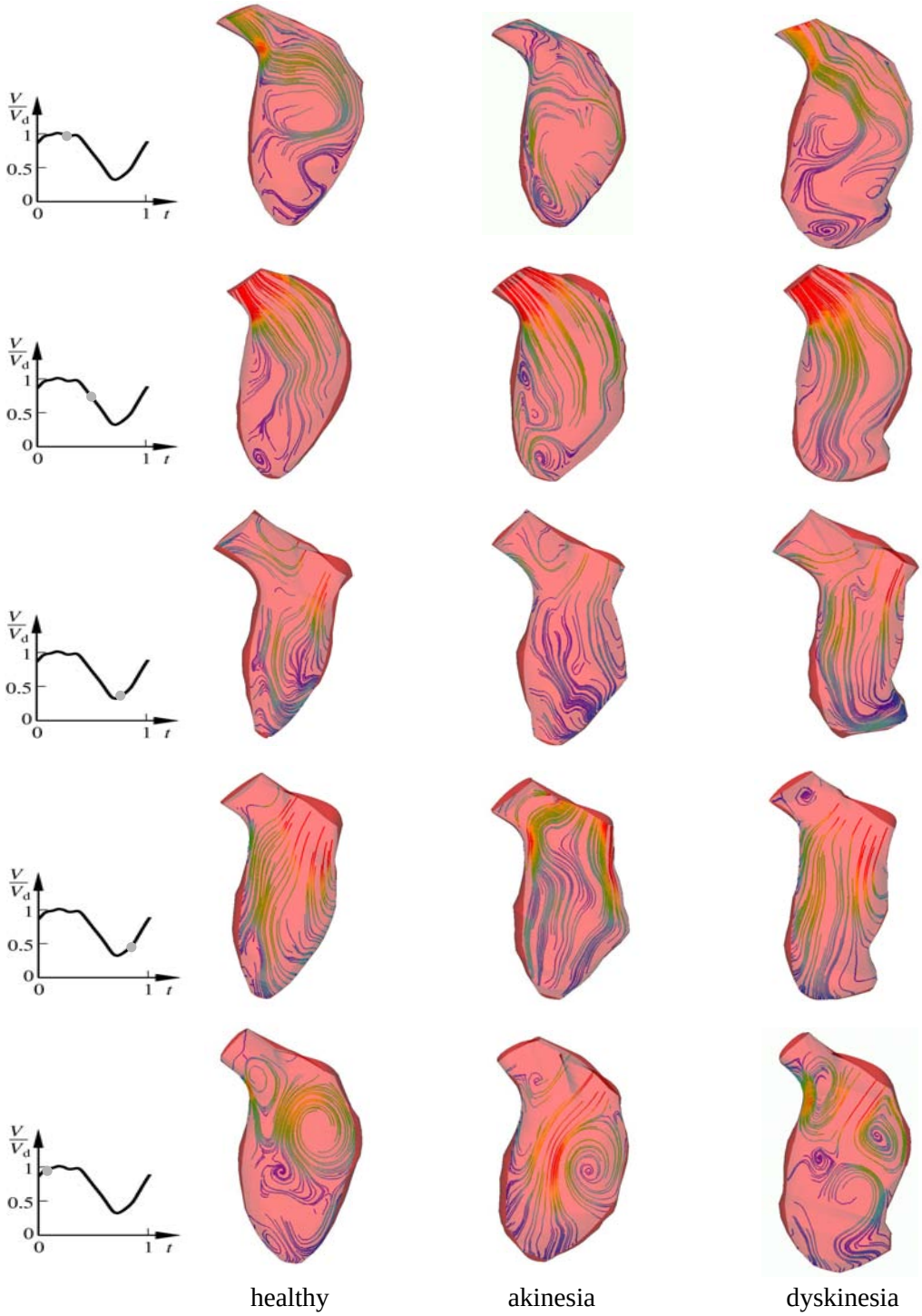

Fig. 37. Flow simulation of pathological ventricle defects $Re_{D,\text{diastolic}} = 1079$, $Re_{D,\text{systolic}} = 2739$, $Wo = 25.2$, $T_0 = 0.77$ s

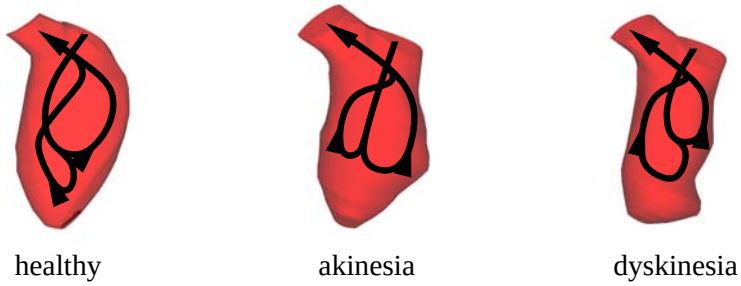

Fig. 38. Cardiac flow in the healthy and pathological left ventricle

flow already has the correct direction before it is expelled, the fluid can flow out without changing its direction. In this manner, the fluid passes through the ventricle smoothly, without having to overcome deceleration and acceleration phases as its direction changes. Figure 38 shows the main path of the blood flow. The greater part of the fluid moves on one of these paths during one cycle. The blood is caught by one of these vortices and transported via the aortic valve into the circulatory system. If the blood reaches the right-hand path, it generally remains in the right half of the ventricle and is led from there to the exit. However, if the fluid particle is found in the left-hand part of the vortex, as the vortex splits it passes either to the lower part of the ventricle or to the aortic exit.

The main flow direction of dyskinesia is also prescribed by a ring vortex. The right-hand path of the blood flow is not so well defined as for the healthy ventricle. Therefore no flow reaches and passes through the dilatated region. A further flow path goes through the lower part of the heart. The vortex passing into the middle orientates itself in the direction of the aortic exit and the fluid can pass out unhindered. The flow in an aneurism, just as in the other two flows, is defined by a ring vortex. However, the flow divides itself into the right-hand and left-hand part of the ventricle. In addition, the ring vortex remains horizontal in the ventricle, i.e. it does not moves to the top of the ventricle. The consequence of this is an insufficient rinsing out of the top of the ventricle. The orientation of the increasing right-hand vortex in the ventricle does not immediately find the direction to the aortic exit during the diastole. At the start of the systole, the right-hand part of the ring vortex has found its direction and flows out.

4.2 Further Model Developments

As the KAHMO heart model is further developed, it will retain the advantage that pathological hearts with ventricle defects can be treated based on MRT data images without knowing the myocardial structure of the human heart. It is only for the relaxation phase of the cardiac cycle in the diastole that

the flow-structure coupling with the myocardium of the ventricle is taken into account. Instead of the partition in the coupling of the aorta motion in Chapter 3, a direct flow-structure coupling will be developed. The structure data of the myocardium during the filling phase of the heart necessary to do this will be taken from the myocardium model of Nash and Hunter (2000), based on stress-extension measurements on animal hearts.

The direct flow-structure coupling was initially performed for an ellipsoidal heart geometry and a time-varying modulus of elasticity of the myocardium material. The nonlinear and anisotropic material properties and the large deformation of the flexible myocardium during the filling phase of the heart are now taken into account. The flow-structure simulation of the model ventricle takes place in four steps.

The main idea of the approach is to get the spatial and temporal distributions of pressure and velocity within the ventricle by means of fitting the real human ventricular pressure-volume loop, where the key point is to obtain a fictitious time-varying Young's modulus of the ventricular wall, namely the Young's modulus time curve. In the second step, based on the obtained p–V curves of different Young's moduli, interpolation is performed to get the fictitious Young's modulus time curve that fits the prescribed p–V curve of the filling phase. In the third step, the fluid-structure coupled simulation is performed by introducing the fictitious Young's modulus time curve into the heart model and imposing the transmitral velocity history is on the mitral orifice position. In the final fourth step, based on the results of coupled simulations, the relation curve of average intraventricular pressure and ventricular volume is obtained and compared with the target p–V curve. The Young's modulus time curve is then improved until the simulated p–V curve matches the target curve. Figure 39 shows the flow-structure simulation of the ellipsoidal model ventricle. The same flow structure is seen during the diastolic filling phase as has been described in Chapter 2.

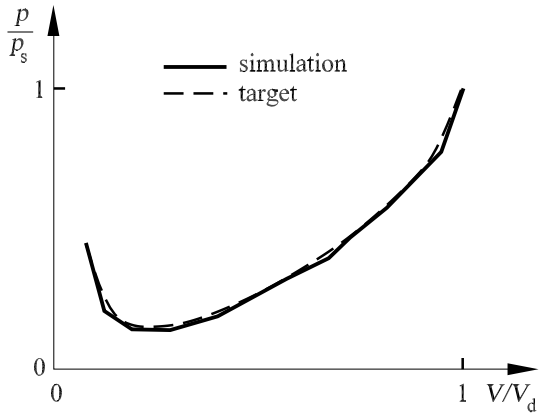

Fig. 39. Pressure-volume relation of an ellipsoidal model ventricle

Acknowledgements

This work was made possible by the enthusiastic and constructive collaboration of the KAHMO heart development team of T. Schenkel, S. Donisi, M. Malve and M. Reik of the Institute for Fluid Mechanics at the University of Karlsruhe. We appreciate the support of B. Jung and W. Schiller for taking the MRT images at the University Hospitals of Freiburg and Bonn, as well as R. Schwarz for converting the images at the Fraunhofer Institute for Applied Information Technology. D. Liepsch and T. Schmidt are thanked for carrying out the validation experiment at Munich University of Applied Sciences. The author would also like to acknowledge his collaboration with F. Beyersdorf and A. Geibel from the Department of Cardiovascular Surgery at the University Hospital, Freiburg, who gave important impulses with their medical advice. My special thanks to K. Mayes for the help preparing this manuscript.

References

Beyersdorf F., 2003. *Private comunications*. Department of Cardiovascular Surgery, Universitätsklinikum Freiburg.

Cheng, Y., Oertel H., Zrcher L., Schenkel T., 2003. *3 D CFD Simulation of Pulsatile Blood Flow in the Human Aorta*. Chinese J. of Biomedical Engineering, **12, 4**, 174–183

Cheng, Y., Schenkel T., Oertel H., 2004. *Fluid-Structure Coupled Simulation of the Left Ventricular Flow During the Filling Phase*. J. of Biomechanics and Modeling in Mechanobiology, accepted

Computational Dynamics Limited, 2003. *StarCD User Guide*. Techn. Report, London.

Dijkstra.E.W., 1959. *A Note on Two Problems in Connexion with Graphs*. Num. Math., **1**, 269–271

Fraunhofer Institute for Algorithms and Scientific Computing, 2000. *User s Guide for the MpCCI Visualiser*. Techn. Report, Sankt Augustin.

Fung Y.C., 1997. *Biomechanics: Circulation*. 2nd edn., Springer-Verlag, Berlin, Heidelberg, New York.

Guyton A.C., Coleman T.G., Granger H.J., 1972. *Circulation: Overall Regulation*. Ann. Rev. Physiologie, **34**, 13–46

Handke M., Jahnke C., Heinrichs G., Schlegel J., Vos C., Schmitt D., Bode C., Geibel A., 2003. *New Three-Dimensional Echocardiographic System Using Digital Radiofrequency Data-Visualization and Quantitative Analysis of Aortic Valve Dynamics With High Resolution*. Circulation, **107**, 2876–2879

Hunter P.J., McCulloch A.D., ter Keurs H.E.D.J., 1998. *Modelling the Mechanical Properties of Cardiac Muscle*. Progr. in Biophysics and Molecular Biology, **69**, 289–331

Hunter P.J., Nash M.P., Sands G.B., 1996. *Computational Electromechanics of the Heart*. In: Computational Biology of the Heart. Eds. Panfilov A.V., Holden A.V., John Wiley & Sons, Chichester, New York, 345–407

Hunter P.J., Smaill B.H., Nielsen P.M.F., LeGrice I.J., 1996. *A Mathematical Model of Cardiac Anatomy*. In: Computational Biology of the Heart. Eds. Panfilov A.V., Holden A.V., John Wiley & Sons, Chichester, New York, 171–215

INTES, 2000. *Permas User Guide*. Techn. Report, Suttgart.

Jung B., 2003. *Private comunications*. Department of Cardiovascular Surgery, Universitätsklinikum Freiburg.

Lemmon J.D., Yoganathan A.P., 2000. *Three-Dimensional Computational Model of Left Heart Diastolic Function with Fluid-Structure Interaction*. J. of Biomech. Eng., **122**, 109–117

Liepsch D., Thursten G., Lee M., 1991. *Studies of Fluids Simulating Blood-like Rheological Properties and Applications in Models of Arterial Branche*. Biorheology, **28**, 39–624

Liepsch D, Moravec S., Baumgart R., 1992. *Some Flow Visualization and Laser-Doppler Velocity Measurements in a True-to-Scale Elastic Model of a Human Aortic Arch — A new model technique*. Biorheology, **29**, 563–680

Mortensen E.N.,Barrett W.A., 1998. *Interactive Segmentation with Intelligent Scissors*. raphical Models and Image Processing, **60**, **5**, 349–384

McQueen D.M., Peskin C.S., 2001. *Heart Simulation by an Immersed Boundary Method with Formal Second Order Accuracy and Reduced Numerical Viscosity*. In: Mechanics for a New Millennium, Proceedings of the 20th ICTAM, Chicago, Illinois. Eds. Aref H., Phillips, J.W., Kluwer Academic Publishers, Dordrecht, Norwell, Massachusetts

Nash M. P., Hunter P.J., 2000. *Computational mechanics of the heart*. J. of Elasticity, **61**, 113–141

Naujokat E., Kiencke U., 2000. *Neuronal and Hormonal Cardiac Control Processes in a Model of the Human Circulatory System*. Int J. of Bioelectromagnetism, **2**, **2**, 1–7

Oertel H., 2004. *Biofluid Mechanics of Blood Circulation*. In: Prandtl's Essentials of Fluid Mechanics. Ed. Oertel H., Springer-Verlag, New York, 615–654

Oertel H., Böhle M., 2004. *Strömungsmechanik*. 3rd edn., Vieweg-Verlag, Wiesbaden

Oertel H., Laurien E., 2003. *Numerische Strömungsmechanik*. 2nd edn., Vieweg-Verlag, Wiesbaden

Oertel H., Schenkel T., Donisi S., Reik M., 2004. *KAHMO — Karlsruhe Heart Model*. Techn. Report, Institute for Fluid Mechanics, University of Karlsruhe, **1**

Pasipoularides A.D., Shu M., Womack M.S., Shah A., von Ramm O., Glower D.D., 2003. *RV Functional Imaging: 3-D Echo-Derived Dynamic Geometry and Flow Field Simulations*. Am. J. of Physiol., **284**, 56–65

Perktold K., Resch M., Florian H., 1991. *Pulsatile non–Newtonian Flow Characteristics in a Three-dimensional Human Carotid Bifurcation Model*. J. of

Biomech. Eng., **113**, 464–475

Peskin C.S., McQueen D.M., 1997. *Fluid Dynamics of the Heart and its Valves*. In: Case Studies in Mathematical Modeling — Ecology, Physiology, and Cell Biology. Eds. Othmer H.G., Adler F.R., Lewis M.A., Dallon J.C., Prentice-Hall, Englewood Cliffs, New Jersey, 309–337

Robb J. S., Robb R.C., 1942. *The normal heart: Anatomy and Physiology of the Structural Units*. Am. Heart J., **23**, 455–467

Schenkel T., Donisi S., Strein S., Oertel H., 2004. *Simulation of Left Ventricle Flow: Application to Generic Pathologies*. J. of Biomechanics, submitted

Schenkel T., Keber R., Oertel H., 2003. *Flow in a Pumping Human Ventricle*. In: Physics and Engineering in Evidence–Based Medicine. Proceedings of the World Congress on Medical Physics and Biomedical Engineering, Sydney. Eds. Allen B., Lovell N., **5**, 1–3

Schenkel T., Meyer S., Oertel H., 2003. *Human Model Aorta*. In: Physics and Engineering in Evidence–Based Medicine. Proceedings of the World Congress on Medical Physics and Biomedical Engineering, Sydney. Eds. Allen B., Lovell N., **138**, 1–3

Schiller W., 2002. *Private comunications*. Universitätsklinikum Bonn.

Schwarz R., 2003. *Semiautomatische Segmentierung des linken Herzventrikels für Strömungssimulationen*. Techn. Report, Fraunhofer-Institut für Angewandte Informationstechnik, Sankt Augustin, 1–6

Watanabe H., Hisada T., Sugiura S., Okada J., Fukunari H., 2002. *Computer Simulation of Blood Flow, Left Ventricular Wall Motion and their Interrelationship by Fluid-Structure Interaction Finite Element Method*. JSME, C, **45**, **4**, 1003–1012